Available online www.jsaer.com

***Journal of Scientific and Engineering Research*, 2017, 4(12):302-339**

Research Article

ISSN: 2394-2630
CODEN(USA): JSERBR

Spectral Method Applied to Thermochemical Non-Equilibrium Reentry Flows in 2D: Seven Species – High Order Analysis

Edisson Sávio de Góes Maciel

Instituto Tecnológico de Aeronáutica (ITA) – Rua Santa Clara, 245 – Cx. Postal: 2029, 12.243-970 – São José dos Campos – SP – Brazil

Abstract In the present work, a study involving a spectral method to solve the reactive Euler and Navier-Stokes equations is performed. The Euler and Navier-Stokes equations, in conservative and finite volume contexts, employing structured spatial discretization, on a condition of thermochemical non-equilibrium, are studied. The spectral method presented in this work employs collocation points and variants of Chebyshev and Legendre interpolation functions are analyzed. High-order studies are accomplished to verify the accuracy of the spectral method. The "hot gas" hypersonic flows around a blunt body, around a double ellipse, and around a reentry capsule in two-dimensions are performed. The Van Leer and the Liou and Steffen Jr. flux vector splitting algorithms are applied to execute the numerical experiments. The Euler backward integration method is employed to march the schemes in time. The convergence process is accelerated to steady state condition through a spatially variable time step procedure, which has proved effective gains in terms of computational acceleration (see Maciel). The reactive simulations involve Earth atmosphere chemical model of seven species and eighteen reactions, based on the Blottner model. N, O, N_2, O_2, NO, NO^+, and e^- species are used to accomplish the numerical comparisons. The results have indicated that the Chebyshev collocation point variants are more accurate in terms of stagnation pressure estimations. In the inviscid case such errors were inferior to 16.16%, while in the viscous case such errors were inferior to 10.0%. The Legendre collocation point variants are more accurate in terms of the lift coefficient estimations. Moreover, the Legendre collocation point variants are more computationally efficient and cheaper.

Keywords Hypersonic flow; thermochemical non-equilibrium reentry flows; reactive Euler and Navier-Stokes equations; high order accuracy; Van Leer scheme; Liou and Steffen Jr. scheme; spectral method.

1. Introduction

There are several approaches for computationally modeling fluid dynamics. These include finite difference, finite element, and spectral methods to name a few. Finite element and finite difference methods are frequently used and offer a wide range of well-known numerical schemes. These schemes can vary in terms of computational accuracy but are typically of lower order of accuracy. If a more accurate solution is desired, it is common practice to refine the mesh either globally or in a region of interest. This can often be a complicated or time consuming process as global mesh refinement will greatly increase the computation time while local refinement requires an elaborated refinement operation [1].

Alternatively, polynomial refinement has been used to improve the solution accuracy and has been shown to converge more quickly than mesh refinement in some cases [2-3]. For finite difference methods, polynomial refinement is performed by including neighboring node values in a higher order polynomial [4]. This can increase the complexity of the scheme especially near the boundaries where nodes do not exist to construct the

higher order polynomials. Finite element methods instead increase the number of unknown values within the cell itself to construct a higher order solution [5].

A scheme with a very high formal order of accuracy will not necessarily always produce the highest resolution. [6] demonstrated that a spectral-like scheme with a formal fourth-order accuracy produced a much more highly resolved solution than schemes with higher formal orders of accuracy when comparing modified wave numbers. Therefore, formal order of accuracy does not provide a comprehensive basis for selecting the best solution procedure. State-of-art methods such as spectral methods fall into this category.

Spectral methods are considered a class of solution techniques using sets of known functions to solve differential equations [7]. Such methods are generally considered high order and capable of obtaining solutions with a high resolution. Unlike finite-difference and finite-element methods, spectral methods utilize an expansion in terms of global, rather than local, basis functions to represent the solution of a differential equation. When properly applied, these techniques accurately resolve phenomena on the scale of the mesh spacing. The order of truncation error decay with mesh refinement is also higher than which can be achieved with finite-difference and finite-element methods. For problems with smooth solutions, it is possible to produce spectral method whose truncation error goes to zero as faster than any finite power of the mesh spacing (exponential convergence).

Spectral methods may be viewed as an extreme development of the class of discretization schemes known by the generic name of method of weighted residuals (MWR) [8]. The key elements of the MWR are the trial functions (also called the expansion or approximating functions) and the test functions (also known as weighted functions). The trial functions are used as the basis functions for a truncated series expansion of the solution that, when substituted into the differential equation, produces the residual. The test functions are used to enforce the minimization of the residual.

The choice of the trial functions is what distinguishes the spectral methods from the element and finite difference methods. The trial functions for spectral methods are infinitely differentiable global functions (Typically, they are tensor products of the eigen functions of singular Sturm-Liouville problems). In the case of finite element methods, the domain is divided into small elements and a trial function is specified in each element. The trial functions are thus local in character and well suited for handling complex geometries. The finite difference trial functions are likewise local.

The choice of test function distinguishes between Galerkin and collocation approaches. In the Galerkin approach, the test functions are the same as the trial functions, whereas in the collocation approach the test functions are translated Dirac delta functions. In other words, the Galerkin approach is equivalent to a least-square approximation, whereas the collocation approach requires the differential equations to be solved exactly at the collocation points.

The collocation approach is the simplest of the MWR and appears to have been first used by [9] in his study of electronic energy bands in metals. A few years later, [10] applied this method to the problem of torsion in square prism. [11] developed it as a general method for solving ordinary differential equations. They used a variety of trials functions and an arbitrary distribution of collocation points. The work of [12] established for the first time that a proper choice of the trial functions and the distribution of collocation points is crucial to the accuracy of the solution. Perhaps he should be credited with laying down the foundation of the orthogonal collocation method.

Spectral methods have been used on one-dimensional, compressible flow problems with piecewise linear solutions by [13-14]. These reports demonstrated that spectral methods, when combined with appropriate filtering techniques, can capture one-dimensional shock waves in otherwise featureless flows. A different sort of demonstration was provided by [15]. They exhibited spectral solutions of compressible flows with nontrivial structures in the smooth regions.

Renewed interest in the area of hypersonic flight has brought Computational Fluid Dynamics (CFD) to the forefront of fluid flow research [16]. Many years have seen a quantum leap in advancements made in the areas of computer systems and software which utilize them for problem solving. Sophisticated and accurate numerical algorithms are devised routinely that are capable of handling complex computational problems. Experimental test facilities capable of addressing complicated high-speed flow problems are still scarce because they are too

expensive to build and sophisticated measurements techniques appropriate for such problems, such as the non-intrusive laser, are still in the development stage. As a result, CFD has become a vital tool in the flow problem solution.

In high speed flows, any adjustment of chemical composition or thermodynamic equilibrium to a change in local environment requires certain time. This is because the redistribution of chemical species and internal energies require certain number of molecular collisions, and hence a certain characteristic time. Chemical non-equilibrium occurs when the characteristic time for the chemical reactions to reach local equilibrium is of the same order as the characteristic time of the fluid flow. Similarly, thermal non-equilibrium occurs when the characteristic time for translation and various internal energy modes to reach local equilibrium is of the same order as the characteristic time of the fluid flow. Since chemical and thermal changes are the results of collisions between the constituent particles, non-equilibrium effects prevail in high-speed flows in low-density air.

In chemical non-equilibrium flows the mass conservation equation is applied to each of the constituent species in the gas mixture. Therefore, the overall mass conservation equation is replaced by as many species conservation equations as the number of chemical species considered. The assumption of thermal non-equilibrium introduces additional energy conservation equations – one for every additional energy mode. Thus, the number of governing equations for non-equilibrium flow is much bigger compared to those for perfect gas flow. A complete set of governing equations for non-equilibrium flow may be found in [17-18].

The problems of chemical non-equilibrium in the shock layers over vehicles flying at high speeds and high altitudes in the Earth's atmosphere have been discussed by several investigators [19-22]. Most of the existing computer codes for calculating the non-equilibrium reacting flow use the one-temperature model, which assumes that all of the internal energy modes of the gaseous species are in equilibrium with the translational mode [21-22]. It has been pointed out that such a one-temperature description of the flow leads to a substantial overestimation of the rate of equilibrium because of the elevated vibrational temperature [20]. A three-temperature chemical-kinetic model has been proposed by [23] to describe the relaxation phenomena correctly in such a flight regime. However, the model is quite complex and requires many chemical rate parameters which are not yet known. As a compromise between the three-temperature and the conventional one-temperature model, a two-temperature chemical-kinetic model has been developed ([24-25]), which is designated herein as the TTv model. The TTv model uses one temperature T to characterize both the translational energy of the atoms and molecules and the rotational energy of the molecules, and another temperature Tv to characterize the vibrational energy of the molecules, translational energy of the electrons, and electronic excitation energy of atoms and molecules. The model has been applied to compute the thermodynamic properties behind a normal shock wave in a flow through a constant-area duct [24-25]. Radiation emission from the non-equilibrium flow has been calculated using the Non-equilibrium Air Radiation (NEQAIR) program [26-27]. The flow and the radiation computations have been packaged into a single computer program, the Shock-Tube Radiation Program (STRAP) [25].

In the present work, a study involving a spectral method to solve the reactive Euler and Navier-Stokes equations is performed. The Euler and Navier-Stokes equations, in conservative and finite volume contexts, employing structured spatial discretization, on a condition of thermochemical non-equilibrium, are studied. The spectral method presented in this work employs collocation points and variants of Chebyshev and Legendre interpolation functions are analyzed. High-order studies are accomplished to verify the accuracy of the spectral method. The "hot gas" hypersonic flows around a blunt body, around a double ellipse, and around a reentry capsule in two-dimensions are performed. The [28-29] flux vector splitting algorithms are applied to execute the numerical experiments. The Euler backward integration method is employed to march the schemes in time. The convergence process is accelerated to steady state condition through a spatially variable time step procedure, which has proved effective gains in terms of computational acceleration [30-31]. The reactive simulations involve Earth atmosphere chemical model of seven species and eighteen reactions, based on the [32] model. N, O, N_2, O_2, NO, NO^+, and e^- species are used to accomplish the numerical comparisons. The results have indicated that the Chebyshev collocation point variants are more accurate in terms of stagnation pressure estimations. In the inviscid case such errors were inferior to 16.16%, while in the viscous case such errors were

inferior to 10.0%. The Legendre collocation point variants are more accurate in terms of the lift coefficient estimations.

2. Spectral Method

Two classes of techniques for spectral discretization are referred to as tau and collocation methods [33]. The latter technique is used here. In this scheme, the approximation series is determined by satisfying the differential equation exactly at a set of distinct collocation points. The locations of these points in the domain are linked to the choice of basis function. In this study, arbitrary collocation points are implemented. The collocation method is used here since enforcement of boundary conditions and evaluations of nonlinear terms are straightforward. Additionally, some accuracy advantage is seen in the collocation method over the tau method for a number of problems [33]. The series expansion for a function Q(x) may be represented as

$$Q_N(x) = \sum_{n=0}^{N} \hat{Q}_n B_n(x), \tag{1}$$

Where $B_n(x)$ are the basis functions and N is the total number of nodes employed in the interpolation process (It is also the order of accuracy of the spectral method). The coefficients $\hat{Q}_n$ are often termed the spectrum of $Q_N(x)$. One common technique used to evaluate the spectrum is to consider Eq. (1) as an interpolation series representing Q(x). The interpolation "nodes" of such series are the collocation points of the method. For a scheme based on Chebyshev collocation, the basis functions are:

$$B_n(x) = T_n(x) = 2xP_{n-1}(x) - P_{n-2}(x), \; n \geq 2, \tag{2}$$

with: $P_0(x) = 1$ and $P_1(x) = x$. The Chebyshev-Gauss-Lobatto standard collocation points are

$$x_l = \cos\left(\frac{\pi l}{N}\right), \qquad l = 0, 1, \ldots, N. \tag{3}$$

The Chebyshev collocation points result from a simple change of variables, which relates the Chebyshev interpolation series to a Fourier cosine series [33]. To evaluate the $\hat{Q}_n$, the inverse relation is required. This is

$$\hat{Q}_n = \hat{c}_n \sum_{l=0}^{N} w_l B_n(x_l) Q_{i,j}, \qquad n = 0, 1, \ldots, N, \tag{4}$$

With w_l being a normalized weighting function and $\hat{c}_n$ a constant. These variables assume the following expressions to a Chebyshev-Gauss-Lobatto interpolation:

$$\hat{c}_n = \frac{2}{N\bar{c}_n}, \text{ where: } \bar{c}_n = \begin{cases} 2, & n = 0 \text{ or } N \\ 1, & 1 < n < N-1 \end{cases}; \text{ and } \quad w_l = \frac{1}{\bar{c}_l}. \tag{5}$$

Legendre collocation is based on using Legendre polynomials as the basis function in Eq. (1), e.g.,

$$B_n(x) = \left[(2n-1)xP_{n-1}(x) - (n-1)P_{n-2}(x)\right]/n, \; n \geq 2, \tag{6}$$

where: $P_0(x) = 1$ and $P_1(x) = x$. Interpolation via Legendre series cannot easily be related to trigonometric interpolation, so there is no simple expression to evaluate the $\hat{Q}_n$ coefficients. Appeal must be made to the theory of numerical quadrature to form an approximation to the integrals which result from analytic Legendre interpolation [34]. Considering Eq. (4), the normalized weights and constant of the Legendre-Gauss-Lobatto collocation points are

$$w_l = \frac{1}{N(N+1)B_N^2(x_l)} \text{ and } \hat{c}_n = \begin{cases} 2n+1, & n = 0,1,\ldots,N-1 \\ N, & n = N \end{cases}. \tag{7}$$

In this work, it was assumed that the Legendre-Gauss-Lobatto collocation points are the same as the Chebyshev-Gauss-Lobatto ones. It was also adopted the following collocation points and normalized weight for the Chebyshev-Gauss-Radau interpolation, based on the work of [35]:

$$x_l = \cos\left(\frac{2\pi l}{2N+1}\right), \tag{8}$$

$$w_l = \begin{cases} \frac{N}{2N+1}, & l = 0 \\ \frac{N}{N+1}, & \text{elsewhere} \end{cases}. \tag{9}$$

For the Legendre-Gauss-Radau interpolation, also based in [35], the collocation points are defined by Eq. (8) and the normalized weights are described by:

$$w_l = \begin{cases} \dfrac{1}{(N+1)^2}, & l = 0 \\ \dfrac{1}{2(N+1)^2} \times \dfrac{1-x_l}{B_N(x_l)}, & \text{elsewhere} \end{cases}. \quad (10)$$

The same calculation to the vector of conserved variables Q is applied to the vector of flux C, to be defined in section 4.

Hence, we have two collocation point options and two normalized weight functions to be considered by the Chebyshev and the Legendre methods, namely: Chebyshev-Gauss-Radau, Chebyshev-Gauss-Lobatto, Legendre-Gauss-Radau and Legendre-Gauss-Lobatto.

3. Reactive Navier-Stokes Equations in 2D

As the Navier-Stokes equations tend to the Euler equations when high Reynolds number are employed, only the former equations are presented. The reactive Navier-Stokes equations in thermochemical non-equilibrium, where the rotational and vibrational contributions are considered, were implemented on conservative and finite volume contexts, in the two-dimensional space. In this case, these equations in integral and conservative forms can be expressed by:

$$\frac{\partial}{\partial t}\int_V Q dV + \int_S \vec{F} \bullet \vec{n} dS = \int_V S_{CV} dV \text{, with: } \vec{F} = (E_e - E_v)\vec{i} + (F_e - F_v)\vec{j}, \quad (11)$$

where: Q is the vector of conserved variables, V is the volume of a computational cell, $\vec{F}$ is the complete flux vector, $\vec{n}$ is the unity vector normal to the flux face, S is the flux area, S_{CV} is the chemical and vibrational source term, E_e and F_e are the convective flux vectors or the Euler flux vectors in the x and y directions, respectively, and E_v and F_v are the viscous flux vectors in the x and y directions, respectively. The $\vec{i}$ and $\vec{j}$ unity vectors define the Cartesian coordinate system. Eleven (11) conservation equations are solved: one of general mass conservation, two of linear momentum conservation, one of total energy, six of species mass conservation, and one of the vibrational internal energy of the molecules. Therefore, one of the species is absent of the iterative process. The CFD literature recommends that the species of biggest mass fraction of the gaseous mixture should be omitted, aiming to result in a minor numerical accumulation error. To the present study, in which is chosen a chemical model to the air composed of seven (7) chemical species (N, O, N_2, O_2, NO, NO^+, and e^-) and eighteen chemical reactions to the [32] model, this species can be the N_2 or the O_2. To this work, the N_2 was chosen. The vectors Q, E_e, F_e, E_v, F_v, and S_{CV} can, hence, be defined as follows:

$$Q = \begin{Bmatrix} \rho \\ \rho u \\ \rho v \\ e \\ \rho_1 \\ \rho_2 \\ \rho_4 \\ \rho_5 \\ \rho_6 \\ \rho_7 \\ \rho e_V \end{Bmatrix}, E_e = \begin{Bmatrix} \rho u \\ \rho u^2 + p \\ \rho uv \\ \rho Hu \\ \rho_1 u \\ \rho_2 u \\ \rho_4 u \\ \rho_5 u \\ \rho_6 u \\ \rho_7 u \\ \rho e_V u \end{Bmatrix}, F_e = \begin{Bmatrix} \rho v \\ \rho uv \\ \rho v^2 + p \\ \rho Hv \\ \rho_1 v \\ \rho_2 v \\ \rho_4 v \\ \rho_5 v \\ \rho_6 v \\ \rho_7 v \\ \rho e_V v \end{Bmatrix}, E_v = \frac{1}{Re}\begin{Bmatrix} 0 \\ \tau_{xx} \\ \tau_{xy} \\ f_x - \phi_x \\ -\rho_1 v_{1x} \\ -\rho_2 v_{2x} \\ -\rho_4 v_{4x} \\ -\rho_5 v_{5x} \\ -\rho_6 v_{6x} \\ -\rho_7 v_{7x} \\ q_{v,x} - \phi_{v,x} \end{Bmatrix}, F_v = \frac{1}{Re}\begin{Bmatrix} 0 \\ \tau_{xy} \\ \tau_{yy} \\ f_y - \phi_y \\ -\rho_1 v_{1y} \\ -\rho_2 v_{2y} \\ -\rho_4 v_{4y} \\ -\rho_5 v_{5y} \\ -\rho_6 v_{6y} \\ -\rho_7 v_{7y} \\ q_{v,y} - \phi_{v,y} \end{Bmatrix}; \quad (12)$$

$$S_{CV} = \left\{ 0 \quad 0 \quad 0 \quad 0 \quad \dot{\omega}_1 \quad \dot{\omega}_2 \quad \dot{\omega}_4 \quad \dot{\omega}_5 \quad \dot{\omega}_6 \quad \dot{\omega}_7 \quad \sum_{s=mol} \rho_s \left(e^*_{v,s} - e_{v,s} \right) / \tau_s + \sum_{s=mol} \dot{\omega}_s e_{v,s} \right\}^T ; \tag{13}$$

in which: ρ is the mixture density; u and v are Cartesian components of the velocity vector in the x and y directions, respectively; e is the fluid total energy; H is the total enthalpy; ρ_1, ρ_2, ρ_4,ρ_5, ρ_6, and ρ_7 are densities of the N, O, O_2,NO, NO^+, and e^-, respectively; e_V is the sum of the vibrational energy of the molecules; the τ's are the components of the viscous stress tensor; f_x and f_y are viscous work and Fourier heat flux functions; $\rho_s v_{sx}$ and $\rho_s v_{sy}$ represent the species diffusion flux, defined by the Fick law; ϕ_x and ϕ_y are the terms of mixture diffusion; $\phi_{v,x}$ and $\phi_{v,y}$ are the terms of molecular diffusion calculated at the vibrational temperature; $\dot{\omega}_s$ is the chemical source term of each species equation, defined by the law of mass action; e^*_v is the molecular-vibrational-internal energy calculated with the translational/rotational temperature; τ_s is the translational-vibrational characteristic relaxation time of each molecule; $q_{v,x}$ and $q_{v,y}$ are the vibrational Fourier heat flux components in the x and y directions, respectively; and Re is the laminar Reynolds number.

The viscous stresses, in N/m^2, are determined, according to a Newtonian fluid model, by:

$$\begin{aligned} \tau_{xx} &= \left[2\mu_m \, \partial u/\partial x - 2/3\mu_m \left(\partial u/\partial x + \partial v/\partial y \right) \right]; \\ \tau_{xy} &= \mu_m \left(\partial u/\partial y + \partial v/\partial x \right); \\ \tau_{yy} &= \left[2\mu_m \left(\partial v/\partial y \right) - 2/3\mu_m \left(\partial u/\partial x + \partial v/\partial y \right) \right], \end{aligned} \tag{14}$$

where μ_m is the molecular viscosity. Expressions to f_x and f_y are given below:

$$f_x = \tau_{xx} u + \tau_{xy} v + q_x + q_{v,x}; \tag{15}$$

$$f_y = \tau_{xy} u + \tau_{yy} v + q_y + q_{v,y}, \tag{16}$$

Where q_x and q_y are the Fourier heat flux components and are given by:

$$q_x = k \frac{\partial T}{\partial x} \text{ and } q_y = k \frac{\partial T}{\partial y}. \tag{17}$$

where: k is the thermal conductivity due to translation and rotation. The $q_{v,x}$ and $q_{v,y}$ are the vibrational heat flux components and are given by:

$$q_{v,x} = k_V \, \partial T_V / \partial x \text{ and } q_{v,y} = k_V \, \partial T_V / \partial y, \tag{18}$$

with k_V being the vibrational thermal conductivity and T_V is the vibrational temperature, what characterizes this model as of two temperatures: translational/rotational and vibrational. The terms of species diffusion, defined by the Fick law, to a condition of thermal non-equilibrium, are determined by [36]:

$$\rho_s v_{sx} = -\rho D_s \frac{\partial Y_{MF,s}}{\partial x} \text{ and } \rho_s v_{sy} = -\rho D_s \frac{\partial Y_{MF,s}}{\partial y}, \tag{19}$$

with "s" referent to a given species, $Y_{MF,s}$ being the molar fraction of the species, defined as:

$$Y_{MF,s} = \frac{\rho_s / M_s}{\sum_{k=1}^{ns} \rho_k / M_k} \tag{20}$$

and D_s is the species-effective-diffusion coefficient. "ns" is the number of species. The diffusion terms ϕ_x and ϕ_y which appear in the energy equation are defined by ([37]):

$$\phi_x = \sum_{s=1}^{ns} \rho_s v_{sx} h_s \text{ and } \phi_y = \sum_{s=1}^{ns} \rho_s v_{sy} h_s, \tag{21}$$

Being h_s the specific enthalpy (sensible) of the chemical species "s". The molecular diffusion terms calculated at the vibrational temperature, $\phi_{v,x}$ and $\phi_{v,y}$, which appear in the vibrational-internal-energy equation are defined by [36]:

$$\phi_{v,x} = \sum_{s=mol} \rho_s v_{sx} h_{v,s} \text{ and } \phi_{v,y} = \sum_{s=mol} \rho_s v_{sy} h_{v,s} , \quad (22)$$

With $h_{v,s}$ being the specific enthalpy (sensible) of the chemical species "s" calculated at the vibrational temperature T_V. The sum of Eq. (13), as also those present in Eq. (22), considers only the molecules of the system, namely: N_2, O_2, NO, and NO^+. The laminar Reynolds number is estimated by:

$$Re = \frac{\rho_{char} V_{initial} L_{REF}}{\mu_{m,char}}, \quad (23)$$

With b "char" related to characteristic or free stream variables, $V_{initial}$ is the flow initial velocity, and L_{REF} a characteristic configuration length. For details of the chemical model, the calculation of thermodynamic and transport properties see [38-39].

4. Numerical Algorithms

Considering the two-dimensional and structured case, the flux vector splitting algorithms follow that described in [28-29, 38-39]. The speed of sound is defined by the following expression:

$$a = \sqrt{(\beta+1)\frac{p}{\rho}}, \quad (24)$$

where β is a parameter to be defined, calculated at each interaction.

The system is solved in three parts separately, according to [40]. The first part takes into account the dynamic part, which considers the Navier-Stokes equations, the second one takes into account the chemical part involving the chemical contributions, and finally, the third part considers only the vibrational contribution. Hence, the discrete-dynamic-convective flux, which solves the dynamic part, is given by:

$$R_{i+1/2,j} = |S|_{i+1/2,j} \left\{ \frac{1}{2} M_{i+1/2,j} \left[\begin{pmatrix} \rho a \\ \rho a u \\ \rho a v \\ \rho a H \end{pmatrix}_L + \begin{pmatrix} \rho a \\ \rho a u \\ \rho a v \\ \rho a H \end{pmatrix}_R \right] - \frac{1}{2} \phi_{i+1/2,j} \left[\begin{pmatrix} \rho a \\ \rho a u \\ \rho a v \\ \rho a H \end{pmatrix}_R - \begin{pmatrix} \rho a \\ \rho a u \\ \rho a v \\ \rho a H \end{pmatrix}_L \right] \right\} + \begin{pmatrix} 0 \\ S_x p \\ S_y p \\ 0 \end{pmatrix}_{i+1/2,j}, \quad (25)$$

the discrete-chemical-convective flux is defined by:

$$R_{i+1/2,j} = |S|_{i+1/2,j} \left\{ \frac{1}{2} M_{i+1/2,j} \left[\begin{pmatrix} \rho_1 a \\ \rho_2 a \\ \rho_4 a \\ \rho_5 a \\ \rho_6 a \\ \rho_7 a \end{pmatrix}_L + \begin{pmatrix} \rho_1 a \\ \rho_2 a \\ \rho_4 a \\ \rho_5 a \\ \rho_6 a \\ \rho_7 a \end{pmatrix}_R \right] - \frac{1}{2} \phi_{i+1/2,j} \left[\begin{pmatrix} \rho_1 a \\ \rho_2 a \\ \rho_4 a \\ \rho_5 a \\ \rho_6 a \\ \rho_7 a \end{pmatrix}_R - \begin{pmatrix} \rho_1 a \\ \rho_2 a \\ \rho_4 a \\ \rho_5 a \\ \rho_6 a \\ \rho_7 a \end{pmatrix}_L \right] \right\}, \quad (26)$$

and finally the discrete-vibrational-convective flux is given by:

$$R_{i+1/2,j} = |S|_{i+1/2,j} \left\{ \frac{1}{2} M_{i+1/2,j} \left[(\rho e_v a)_L + (\rho e_v a)_R \right] - \frac{1}{2} \phi_{i+1/2,j} \left[(\rho e_v a)_R - (\rho e_v a)_L \right] \right\}, \quad (27)$$

where: C is the sum of the fluxes at each interface, and $S_{i+1/2,j} = \begin{bmatrix} S_x & S_y \end{bmatrix}^T_{i+1/2,j}$ defines the normal area vector for the surface (i+½,j). The normal area components S_x and S_y to each flux interface are given in Tab. 1. Figure 1 exhibits the computational cell adopted for the simulations, as well its respective nodes and flux interfaces.

The same definitions presented in [28-29, 38-39] are valid to these algorithms. The definition of the dissipation term ϕ determines the particular formulation of the convective fluxes. The choice below corresponds to the [28] scheme, according to [41]:

$$\phi_{i+1/2,j} = \phi^{VL}_{i+1/2,j} = \begin{cases} \left|M_{i+1/2,j}\right|, & \text{if } \left|M_{i+1/2,j}\right| \geq 1; \\ \left|M_{i+1/2,j}\right| + 0.5\left(M_R - 1\right)^2, & \text{if } 0 \leq M_{i+1/2,j} < 1; \\ \left|M_{i+1/2,j}\right| + 0.5\left(M_L + 1\right)^2, & \text{if } -1 < M_{i+1/2,j} \leq 0. \end{cases} \quad (28)$$

and the [29] scheme is obtained by, according to [41]:

$$\phi_{i+1/2,j} = \phi^{LS}_{i+1/2,j} = \left|M_{i+1/2,j}\right|. \quad (29)$$

Both schemes are first-order accurate in space and in time. The high-order spatial accuracy is obtained, in the current study, by the spectral method.

The viscous formulation follows that of [42], which adopts the Green theorem to calculate primitive variable gradients. The viscous gradients at the flux interface are obtained by arithmetical average between cell (i,j) and its neighbors. As was done with the convective terms, there is a need to separate the viscous flux in three parts: dynamic viscous flux, chemical viscous flux, and vibrational viscous flux. The dynamic part corresponds to the first four equations of the Navier-Stokes, the chemical part corresponds to the six equations immediately below the energy equation, and the vibrational part corresponds to the equation that follows the last chemical one. The resultant ordinary differential equation system can be written as:

$$V_{i,j}\, dQ_{i,j}/dt = -\left(R_{i,j-1/2} + R_{i+1/2,j} + R_{i,j+1/2} + R_{i-1/2,j}\right) = -C_{i,j}, \quad (30)$$

where the cell volume is given by:

$$V_{i,j} = 0.5\left|\left(x_{i,j} - x_{i+1,j}\right)y_{i+1,j+1} + \left(x_{i+1,j} - x_{i+1,j+1}\right)y_{i,j} + \left(x_{i+1,j+1} - x_{i,j}\right)y_{i+1,j}\right| +$$
$$0.5\left|\left(x_{i,j} - x_{i+1,j+1}\right)y_{i,j+1} + \left(x_{i+1,j+1} - x_{i,j+1}\right)y_{i,j} + \left(x_{i,j+1} - x_{i,j}\right)y_{i+1,j+1}\right|. \quad (31)$$

In the present study, the Euler backward method was employed to march the scheme in time. This method is first-order accurate in time, to the three types of complete flux. To the convective dynamic component, this method can be represented in general form by:

$$Q^{(n+1)}_{i,j} = Q^{(n)}_{i,j} - \left(\Delta t_{i,j}/V_{i,j}\right) \times C\left(Q^{(n)}_{i,j}\right), \quad (32)$$

to the convective chemical component, it can be represented in general form by:

$$Q^{(n+1)}_{i,j} = Q^{(n)}_{i,j} - \Delta t_{i,j} \times \left[C\left(Q^{(n)}_{i,j}\right)/V_{i,j} - S_C\left(Q^{(n)}_{i,j}\right)\right], \quad (33)$$

where the chemical source term S_C is calculated with the temperature T_{rrc} (reaction rate controlling temperature, see [38-39]). Finally, to the convective vibrational component:

$$Q^{(n+1)}_{i,j} = Q^{(n)}_{i,j} - \Delta t_{i,j} \times \left[C\left(Q^{(n)}_{i,j}\right)/V_{i,j} - S_V\left(Q^{(n)}_{i,j}\right)\right], \quad (34)$$

in which:

$$S_V = \sum_{s=mol} q_{T-V,s} + \sum_{s=mol} S_{C,s} e_{v,s}, \quad (35)$$

Where q_{T-V} is the heat flux due to translational-vibrational relaxation, defined in Eq. (13) and in [38-39].

5. Spatially Variable Time Step

The spatially variable time step has proved efficient gains in terms of convergence acceleration, as verified by [30-31]. Initially, the parameter σ is determined, where:

$$\sigma_s = \frac{c_s}{M_s} \text{ and } \sigma = \sum_{s=1}^{ns} \sigma_s, \quad (36)$$

With c_s being the mass fraction, and M_s the molecular weight. The total specific heat at constant volume due to translation is defined as:

$$c_{V,T} = \sum_{s=1}^{ns} \sigma_s c_{V,T,s}, \quad (37)$$

where, for each gas constituent of the seven (7) species chemical model, the specific heat at constant volume, based on the kinetic theory of gases [43], is defined by

$$c_{V,T,N} = \frac{3}{2}R_N,\ c_{V,T,O} = \frac{3}{2}R_O,\ c_{V,T,N_2} = \frac{5}{2}R_{N_2},\ c_{V,T,O_2} = \frac{5}{2}R_{O_2}, \text{ and } c_{V,T,NO} = \frac{5}{2}R_{NO}; \quad (38)$$

$$c_{V,T,NO^+} = \frac{5}{2}R_{NO^+}, \text{ and } c_{V,T,e^-} = \frac{3}{2}R_{e^-}, \quad (39)$$

Being R_s the specific gas constant. The total pressure of the gaseous mixture is determined by Dalton law, which indicates that the total pressure of the gas is the sum of the partial pressure of each constituent gas, resulting in:

$$p_s = c_s \rho R_s T \text{ and } p = \sum_{s=1}^{ns} p_s . \quad (40)$$

The speed of sound to a reactive mixture can be determined by Eq. (24), where $\beta = \frac{R_{univ}\sigma}{c_{V,T}}$, with R_{univ} = 1.987 cal/(g-mol.K). Finally, the spatially variable time step is defined from the CFL (Courant-Friedrichs-Lewis) definition:

$$\Delta t_{i,j} = \frac{CFL\Delta s_{i,j}}{\sqrt{u_{i,j}^2 + v_{i,j}^2} + a_{i,j}}, \quad (41)$$

where $\Delta s_{i,j}$ is the characteristic length of each cell (defined between the minimum cell side length and the minimum centroid distance between each cell and its neighbors).

6. Dimensionless Scales, Initial and Boundary Conditions

6.1. Dimensionless Scales

The dimensionless scales employed to the reactive equations consisted in: R_s is dimensionless by a_{char}, where $a_{char} = \sqrt{\gamma p_{char}/\rho_{char}}$; c_v is dimensionless by a_{char}; h_s and Δh_s^0 are dimensionless by a_{char}^2; T and T_v, translational/rotational temperature and vibrational temperature, respectively, are dimensionless by a_{char}; ρ_s and ρ are dimensionless by ρ_{char}; u and v are dimensionless by a_{char}; μ is dimensionless by μ_{char}; D, diffusion coefficient, dimensionless by $a_{char}^2\, dt_{char}$, where dt_{char} is the minimum time step calculated in the computational domain at the first iteration; $\dot{\omega}$ is dimensionless by $(\rho_{char}/dt_{char})x10^{-3}$; e_v is dimensionless by a_{char}^2; e and p are dimensionless by $\rho_{char}a_{char}^2$; τ_s, relaxation time, is dimensionless by dt_{char}.The characteristic physical properties are defined in [44].

6.2. Initial Condition

The initial conditions to the blunt body, to the double ellipse, and to the reentry capsule problems, for a seven species chemical model, are presented in Tabs. 2-4. The Reynolds number is obtained from data of [44].

6.3. Boundary Conditions

The boundary conditions are basically of four types: solid wall, entrance, exit, and continuity. These conditions are implemented with the help of ghost cells.

Wall condition. In inviscid case, this condition imposes the flow tangency at the solid wall. This condition is satisfied considering the wall tangent velocity component of the ghost volume as equals to the respective velocity component of its real neighbor cell. At the same way, the wall normal velocity component of the ghost cell is equaled in value, but with opposite signal, to the respective velocity component of the real neighbor cell. It results in:

$$n_x = \Delta y \Big/ \sqrt{\Delta x^2 + \Delta y^2}; \quad \text{and } n_y = -\Delta x \Big/ \sqrt{\Delta x^2 + \Delta y^2}; \tag{42}$$

where, for the (i+1/2,j) interface:

$$\Delta x = x_{i+1,j+1} - x_{i+1,j}; \quad \text{and} \quad \Delta y = y_{i+1,j+1} - y_{i+1,j}. \tag{43}$$

Hence, the ghost cell velocity components are written as:

$$u_g = \left(n_y^2 - n_x^2\right)u_r - \left(2n_x n_y\right)v_r; \quad \text{and} \quad v_g = -\left(2n_x n_y\right)u_r + \left(n_x^2 - n_y^2\right)v_r. \tag{44}$$

with "g" related with ghost cell and "r" related with real cell. To the viscous case, the boundary condition imposes that the ghost cell velocity components be equal to the real cell velocity components, with the negative signal:

$$u_g = -u_r \text{ and } v_g = -v_r. \tag{45}$$

The normal pressure gradient of the fluid at the wall is assumed to be equal to zero according to a boundary-layer like condition. The same hypothesis is applied for the normal temperature gradient at the wall, assuming an adiabatic wall. From the above considerations, density and translational/rotational temperature are extrapolated from the respective values of its real neighbor volume (zero order extrapolation). The total vibrational internal energy is also extrapolated. With the mixture species mass fractions and with the values of the respective specific heats at constant volume, it is possible to obtain the mixture specific heat at constant volume. The mixture formation enthalpy is extrapolated from the real cell. The mixture total energy to the ghost cell is calculated by:

$$e_g = \rho_g \left[c_{v\,mixt,g}\left(T_{tr,g} - T_{REF}\right) + \Delta h^0_{mixt,g} + e_{v,dim,g} + 0.5\left(u_g^2 + v_g^2\right)\right], \tag{46}$$

where: T_{REF}, the reference temperature, Δh^0_{mixt}, mixture formation enthalpy, and $e_{v,dim}$, dimensionless vibrational energy, are defined in [38-39]. To the species density, the non-catalytic condition is imposed, what corresponds to zero order extrapolation from the real cell.

Entrance condition. It is divided in two flow regimes:

(a) Subsonic flow: Three properties are specified and one extrapolated in the boundary conditions of the dynamic part of the [28-29] numerical schemes. This approach is based on information propagation analysis along characteristic directions in the calculation domain [45]. In other words, for subsonic flow, three characteristics propagate information pointing into the computational domain. Thus three flow properties must be fixed at the inlet plane. Just one characteristic line allows information to travel upstream. So, one flow variable must be extrapolated from the interior grid to the inlet boundary. The total energy was the extrapolated variable from the real neighbor volume, for the studied problems. Density and velocity components adopted values of the initial flow. To the chemical part, six information propagate upstream because it is assumed that all six equations are conducted by the eigenvalue "(q_n-a)". In the subsonic flow, all eigenvalues are negative and the information should be extrapolated. In the same reasoning to the chemical boundary conditions, the vibrational-internal-energy equation is dictated by the "(q_n-a)" eigenvalue and, in the subsonic region, its value is negative. Hence, the vibrational internal energy should be extrapolated.

(b) Supersonic flow: In this case no information travels upstream; therefore all variables are fixed with their initial values.

Exit condition It is also divided in two flow regimes:

(a) Subsonic flow: Three characteristics propagate information outward the computational domain. Hence, the associated variables should be extrapolated from interior information. The characteristic direction associated to the "(q_{normal}-a)" velocity should be specified because it points inward to the computational domain [45]. In this case, the ghost volume total energy is specified from its initial value. Density and velocity components are extrapolated. To the chemical part, the eigenvalue "(q_n-a)" is again negative and the characteristics are always flowing into the computational domain. Hence, the six chemical species under study should have their densities

fixed by their initial values. In the same reasoning, the internal vibrational energy should have its value prescribed by its initial value due to the eigenvalue "$(q_n$-a)" be negative.
(b) Supersonic flow: All variables are extrapolated from interior grid cells, as no flow information can make its way upstream. In other words, nothing can be fixed.

Continuity condition. This condition imposes continuity of the flow at the trailing edge of the reentry capsule configuration. This is done considering the Kutta condition in this region. In terms of numerical implementation, it is obtained considering the vector of conserved variables above the wake as equal to the vector of conserved variables below the wake.

7. Physical Problems

Three physical problems were solved in this work, namely: blunt body, double ellipse, and reentry capsule. The first problem considers the geometry of a blunt body with 1.0 m of nose ratio and parallel rectilinear walls. The far field is located at 20.0 times the nose ratio in relation to the configuration nose. A mesh composed of 2,548 rectangular cells and 2,650 nodes was studied for the inviscid case, with an exponential stretching of 5.0% for the viscous case. This mesh is equivalent in finite differences to a one of 53x50 points. Figure 2 shows the detail of the geometry and Figs. 3 and 4 exhibit the inviscid and viscous meshes.
The double ellipse problem is the second under study. The mesh is composed of 4,116 rectangular cells and 4,250 nodes, with an exponential stretching of 5.0% for the viscous case, and far field located at 20.0 unities. This mesh is equivalent in finite differences to a one of 85x50 points. Figure 5 shows the double ellipse geometry and Figs. 6 and 7 exhibit the inviscid and viscous meshes.
The third problem is the geometry of the reentry capsule. Details of the configuration are presented in Fig. 8. The far field is located at 20.0 unities. A mesh of 3,136 rectangular cells and 3,250 nodes was used for the inviscid case, whereas with an exponential stretching of 5.0% was used for the viscous simulations. This mesh is equivalent in finite differences to a one of 65x50 points. Figures 9 and 10 show the inviscid and viscous meshes.

8. Results

Tests were performed in a Core i7 processor of 2.8GHz and 6.0Gbytes of RAM microcomputer, in a Windows 7.0 environment. Three (3) orders of reduction of the maximum residual in the field were considered to obtain a converged solution. The residual was defined as the value of the discretized conservation equation. In the dynamic part of the [28-29] schemes, such definition results in:

$$\text{Residual} = -\Delta t_{i,j} / V_{i,j} \times C_{i,j}. \quad (47)$$

The attack angle was adopted equal to zero. In this work, the inviscid results were obtained for a 4^{th} order of accuracy of the spectral method, whereas the viscous solutions were obtained for an16^{th} order of accuracy of the spectral method. For a matter of simplicity, the following abbreviations were used: [28] scheme = VL, [29] scheme = LS, Chebyshev-Gauss-Radau = CGR, Chebyshev-Gauss-Lobatto = CGL, Legendre-Gauss-Radau = LGR, and Legendre-Gauss-Lobatto = LGL.

8.1. Blunt Body Problem

Inviscid case. Figures 11 to 14 exhibit the pressure and temperature contours obtained by the VL and LS schemes as using the CGR collocation points. The VL algorithm captures a more intense shock than the LS algorithm, as can be seen by the pressure legend. Good symmetry and homogenous properties are observed in the pressure and in the translational/rotational temperature contours. No pre-shock oscillations are observed. The maximum temperature at the configuration nose is 8,470.45K obtained by the VL scheme.
Figures 15 to 18 show the pressure and translational/rotational temperature contours generated by the VL and LS schemes as using CGL collocation points. The maximum pressure is obtained by the LS algorithm, being inferior to that observed in the CGR case. No pre-shock oscillations are observed. The temperature contours presents good symmetry properties. The maximum temperature reaches the value of 8,516.50K and is captured by the VL scheme. The contours are free of oscillations.

Figures 19 to 22 present the pressure and translational/rotational temperature contours calculated by the VL and LS schemes when using the LGR collocation points. The pressure peaks of both solutions are smaller than those obtained in the Chebyshev variants. No pressure oscillations are observed and good symmetry properties are verified. The maximum temperature peak is 8,872.81K, obtained again by the VL scheme. Good symmetry properties are also observed in both temperature contours.

Figures 23 to 26 exhibit the pressure and temperature contours obtained by the VL and LS algorithms when using the LGL collocation points. The pressure peaks are still low. Good symmetry and homogeneous properties are observed and the shock wave is well captured. The temperature contours present also good symmetry properties, free of oscillations. The maximum temperature is obtained by the VL scheme with a value of 8,831.72K.

Viscous case. Figures 27 to 30 present the pressure and temperature contours generated by the VL and LS schemes as using CGR collocation points. The pressure peak values are close to the theoretical stagnation pressure value, with LS scheme being the closest. Good symmetry properties are observed and no pre-shock oscillations are observed. The maximum temperature is calculated with the VL scheme, reaching the mark of 8,762.19K. Good symmetry properties are verified in the temperature field. Note that the heat transfer is better captured by the VL scheme, as can be seen by the contours of temperature close to the configuration wall. The correct transport of properties like viscosity and thermal conduction are qualitatively confirmed.

Figures 31 to 34 show the pressure and translational/rotational temperature contours calculated by the VL and LS algorithms when using CGL collocation points. Again the LS' pressure peak value is very close to the theoretical value of stagnation pressure (see Table 5). The shock wave is well captured by both schemes. Figures 33 and 34 show the translational/rotational temperature contours and the good transport of viscosity and thermal conduction is noted in the VL solution. The maximum temperature is 8,783.18K and is again obtained by the VL scheme; in other words, the VL scheme is being more conservative than the LS scheme.

Figures 35 to 38 exhibit the pressure and temperature contours obtained by the VL and LS algorithms as using the LGR collocation points. Both pressure contours are very similar in qualitative terms, although the pressure peaks are very low. Good symmetry properties are observed in both solutions, free of pre-shock oscillations. Figures 37 and 38 exhibit the temperature contours calculated by the VL and LS schemes, respectively. The temperature field of the VL'ssolution is more intense than that of the LS' solution, reaching a maximum of 9,220.16K. Good symmetry and homogenous properties are observed in both figures.

Figures 39 to 42 present the pressure and translational/rotational temperature contours calculated by the VL and LS algorithms when using the LGL collocation points. Both pressure peak values are reduced in relation to the theoretical stagnation pressure value. Both solutions present good symmetry and homogenous properties, free of oscillations. The shock wave is well captured by both schemes and the transport of viscous properties is well highlighted in the VL's temperature contours. The maximum temperature is obtained by the VL scheme and reaches the value of 9,208.20K.The Legendre solutions present in general higher values to the stagnation temperature than the Chebyshev solutions. In general terms, theChebyshev variants dominate the pressure field, whereas the Legendre variants dominate the temperature field.

8.2. Double Ellipse Problem

Inviscid case. Figures 43 to 46 exhibit the pressure and temperature contours obtained by the VL and LS schemes as using the CGR collocation points. Figures 43 and 44 present the pressure contours, where the LSscheme captures a more intense shock at the bigger ellipse than the VL scheme. Good homogenous properties are observed in the pressure and in the temperature contours. No pre-shock oscillations are observed. The maximum temperature captured by the LS scheme at the configuration nose is 8,843.91K.

Figures 47to 50 show the pressure and translational/rotational temperature contours calculated by the VL and LS schemes as using CGL collocation points. Figures 47 and 48 exhibit the pressure contours of both schemes. The maximum pressure peak is obtained by the LS algorithm. No pre-shock oscillations are observed. Figures 49 and 50 present the temperature contours obtained by both schemes. The maximum temperature reaches the value of 8,948.46K and is captured by the VL scheme. The contours are free of oscillations.

Figures 51 to 54 present the pressure and temperature contours generated by the VL and LS schemes when using the LGR collocation points. Figures 51 and 52 show the pressure contours, where the LS solution is more intense than the VL solution. No pressure oscillations are observed. Figures 53 and 54 exhibit the temperature contours obtained by both schemes. The maximum temperature is 9,271.03K obtained again by the VL scheme. Good homogenous properties are verified in both solutions.

Figures 55 to 58 show the pressure and translational/rotational temperature contours obtained by the VL and LS algorithms when using the LGL collocation points. Figures 55 and 56 exhibit the pressure contours obtained by both algorithms. The pressure field generated by the LS algorithm is more intense than the respective one of the VL algorithm. Good homogeneous properties are observed and the shock waves at the two ellipses are well captured. Figures 57 and 58 present the temperature contours obtained by both algorithms, free of oscillations. The maximum temperature is obtained by the VL scheme with a value of 9,131.99K.

Viscous case. Figures 59 to 62 present the pressure and temperature contours generated by the VL and LS schemes as using CGR collocation points. Figures 59 and 60 show the pressure contours obtained by both schemes. The VL scheme presents the closest pressure peak value in relation to the theoretical stagnation pressure value. No pre-shock oscillations are observed. Figures 61 and 62 exhibit the temperature contours generated by both schemes. The maximum temperature is 9,641.04K calculated with the VL scheme. Good transport of viscous properties is perceptible in the VL's solution. The correct transport of properties like viscosity and thermal conduction are qualitatively confirmed.

Figures 63 to 66 show the pressure and translational/rotational temperature contours calculated by the VL and LS algorithms when using CGL collocation points. Figures 63 and 64 exhibit the pressure contours, where the VL's value of pressure peak is very close to the theoretical value of stagnation pressure. The shock waves are well captured by both schemes. Figures 65 and 66present the translational/rotational temperature contours calculated by both algorithms. The good transport of viscosity and thermal conduction is noted in the VL solution. The maximum temperature is 9,677.41K and is again obtained by the VL scheme.

Figures 67 to 70 exhibit the pressure and temperature contours obtained by the VL and LS algorithms as using the LGR collocation points. Figures 67 and 68 present the pressure contours obtained by both schemes. Both pressure contours are very similar in qualitative terms, being the LS' solution more intense than the respective VL's solution in quantitative terms. Figures 69 and 70 show the temperature contours calculated by the VL and LS schemes, respectively. The maximum temperature in the field is obtained by the VL algorithm and reaches the value of 10,199.80K.

Figures 71 to 74 present the pressure and translational/rotational temperature contours generated by the VL and LS algorithms when using the LGL collocation points. Figures 71 and 72 show the pressure contours, where the LS' field is more intense than the VL's field. The shock waves at the two ellipses are well captured by both schemes. Figures 73 and 74 exhibit the temperature contours, where the maximum temperature in the field is obtained by the VL scheme and reaches the value of 10,209.10K. Good homogeneous properties are observed in both fields.

8.3. Reentry Capsule Problem

Inviscid case. Figures 75 to 78 present the pressure and translational/rotational temperature contours obtained by the VL and LS schemes as using the CGR collocation points. Figures 75 and 76 present the pressure contours and good symmetry and homogenous properties are verified. The stagnation pressure estimated by the LS scheme as using the CGR collocation points is the best in comparison with the CGL, LGR, and LGL solutions, with an error of 4.55%.The Kutta condition was correctly implemented. There are qualitative differences in the pressure contours captured by both schemes. The solution of Figure 75 seems better to represent the normal shock. Figures 77 and 78 present the temperature contours and good symmetry properties are noted. Again, the normal shock seems better captured by the VL solution. The maximum temperature is captured by the LS scheme and has the value of 7,725.38K

Figures 79 to 82 show the pressure and temperature contours generated by the VL and LS numerical algorithms when using the CGL collocation points. Figures 79 and 80 exhibit the pressure contours calculated by both algorithms. The LS' pressure peak is higher than the VL's one. Good symmetry properties are observed in the

pressure and in the temperature contours, free of pre-shock oscillations. The temperature contours are shown in Figs. 81 and 82 and both figures present good symmetry characteristics, without oscillations. The maximum temperature peak is obtained by the LS scheme and has the value of 7,863.71 K.

Figures 83 to 86 exhibit the pressure and translational/rotational temperature contours calculated by the VL and LS algorithms as using the LGR collocation points. Figures 83 and 84 present the pressure contours obtained by the VL and LS algorithms, respectively. The value of stagnation pressure obtained by the LS algorithm is bigger than that of the VL algorithm, although they are very low. As mentioned before, the Legendre variant behaves better for the temperature field and for the determination of the lift aerodynamic coefficient, as seen in Tabs. 8 and 9. Good symmetry properties, without oscillations, are observed in all solutions. The LS algorithm again captures the maximum temperature in the field with a value of 8,058.64K.

Figures 87 to 90 show the pressure and translational/rotational temperature contours obtained by the VL and LS schemes as using the LGL collocation points. Figures 87 and 88 exhibit the pressure contours, where both schemes capture correctly the normal shock wave ahead of the configuration nose. Moreover, the stagnation pressure values of both schemes are under-predicted in relation to the theoretical value. Good symmetry properties are observed. Figures 89 and 90 present the temperature contours obtained by both schemes. Good homogenous properties are verified in the temperature solutions. The trailing edge flow is well captured by the numerical schemes, emphasizing the correct implementation of the Kutta condition. The maximum temperature in the field is calculated by the LS algorithm and reaches the value of 8,012.98K.

Viscous case. Figures 91 to 94 exhibit the pressure and temperature contours calculated by the VL and LS numerical schemes as using the CGR collocation points. Figures 91 and 92 present the pressure contours, where the VL's field is more intense than the LS' field. Good symmetry properties are observed. The dynamic and thermal shock waves are correctly captured by the VL algorithm. Figures 93 and 94 show the temperature contours obtained by the VL and LS schemes, respectively. The maximum stagnation temperature calculated by the VL scheme reaches the value of 8,252.77K.

Figures 95 to 98 show the pressure and translational/rotational temperature contours generated by the VL and LS schemes when using the CGL collocation points. The best result of the reentry-capsule-viscous case for the stagnation pressure was obtained by the LS scheme as using the CGL spectral variant with an error of 1.52%. Again, in general terms, the Chebyshev variants present better behavior when applied to the dynamic part of the flow. Good symmetry properties are verified in the pressure and in the temperature fields. The maximum temperature peak is obtained by the VL scheme and has the value of 8,262.58K

Figures 99 to 102 present the pressure and temperature contours obtained by the VL and LS numerical schemes as using the LGR collocation points. The stagnation pressure values generated by the VL and LS schemes are under-estimated in relation to the theoretical value. The contours are free of pre-shock oscillations and present good homogenous features. Figures 101 and 102 present the temperature contours. The normal thermal shock wave is well captured by the numerical algorithms. Good symmetry properties are observed and the wake is well captured by the numerical schemes, highlighting the correct implementation of the Kutta condition. The maximum temperature in the field is calculated by the VL scheme and has the value of 8,389.48K.

Figures 103 to 106 exhibit the pressure and temperature contours calculated by the VL and LS numerical algorithms when using the LGL collocation points. The stagnation pressure continues under-estimated. Good symmetry properties are verified. The temperature contours are free of oscillations, the wake is well captured by the numerical schemes, and good homogenous properties are noted. The normal thermal shock wave is well captured by the numerical schemes. The maximum temperature in the field is obtained by the VL scheme and reaches the value of 8,389.21K. Again the maximum temperature in the field was predominantly captured by the Legendre variants.

8.4. Other Comparisons

Figure 107 shows the convergence history of the VL scheme to a 4^{th} order spectral method using CGL for collocation points and to an ENO solution also of 4^{th} order using Newton interpolation function, to the blunt body inviscid case. The CGL collocation points were chosen because they provide the best convergence of the VL scheme for the inviscid case and 4^{th} order of accuracy. The ENO procedure was implemented by the author

and was used for numerical comparisons. To details of the implementation of the ENO procedure on a context of thermochemical non-equilibrium, the reader is encouraged to read [46-48]. As can be seen in Fig. 107, the spectral (CGL) method coupled with the VL scheme was the most efficient converging in 222 iterations, with a maximum CFL of 0.70. The ENO solution was very inefficient compared with the spectral method. The maximum allowable CFL number employed in the ENO solutions was 0.01. Figure 108 compares the ENO solution of 4^{th} order using Newton interpolation function, and the spectral (LGR) method, both coupled with the LS scheme. Again, the LGR collocation points were chosen due to provide the best convergence for the LS scheme in the inviscid case and 4^{th} order of accuracy. In this case, the good convergence of the spectral (LGR) method was highlighted, converging in 274 iterations with a CFL number of 0.50, whereas the ENO solutions converged in more than 8,000 iterations with a CFL number of 0.01.

As conclusion, the correct implementation of the proposed spectral method guide us to an efficient high order scheme, converging in less than 300 iterations in the inviscid case, for the blunt body problem, when programmed coupled with the VL or LS schemes. The CGL and LGR variants of the spectral method for the inviscid case were the most efficient in the studies performed by the author and ratified the fast convergence as expected.

8.5. Quantitative Analysis

In order to perform a quantitative analysis, the present reactive results are compared to the perfect gas solutions. The stagnation pressures at the blunt body nose, at the double ellipse nose, and at the reentry capsule nose were evaluated assuming the perfect gas formulation. Such parameter calculated at this way is not the best comparison, but in the absence of practical reactive results, this constitutes the best available solution.

To calculate the stagnation pressure at the nose of these three configurations, [49] presents in its B Appendix values of the normal shock wave properties ahead of the configuration. The ratio pr_0/pr_∞ is estimated as function of the normal Mach number and the stagnation pressure pr_0 can be determined from this parameter. Hence, Table 5 gives the theoretical stagnation pressure values obtained for the three configurations at the initial-normal-Mach number.The value of pr_∞ is determined by the following expression:

$$pr_\infty = \frac{pr_{initial}}{\rho_{char} \times a_{char}^2}, \tag{48}$$

where, for example, for the blunt body case, $pr_{initial}$ = 687N/m^2, ρ_{char} = 0.004kg/m^3 and a_{char} = 317.024m/s. Considering these values, one concludes that pr_∞ = 1.709 (non-dimensional). Using the ratio obtained from [49], the stagnation pressure ahead of the configuration nose is estimated as 170.87 unities. Tables 6 (inviscid case) and 7 (viscous case) compare values of the stagnation pressure obtained from the simulations with the theoretical values and show the percentage errors. As can be seen, the best results in the inviscid case are provided by the CGR collocation points, with an error of 0.23%, when coupled with the VL scheme, for the blunt body problem; by the CGR collocation points, with an error of 2.71%, when coupled with the LS scheme, for the double ellipse problem; and by CGL collocation points, with an error of 4.55%, when coupled with the LS scheme, for the reentry capsule problem. For the viscous case, the CGL collocation points, with an error of 1.38%, coupled with the LS scheme, for the blunt body problem, was the best; with the CGR collocation points, with an error of 0.28%, coupled with the VL scheme, for the double ellipse problem, was the best; and with the CGL collocation points, with an error of 1.52%, coupled with the LS scheme, for the reentry capsule problem, was the best.

As the hypersonic flows around the blunt body and reentry capsule configurations were simulated with a zero value to the attack angle, a zero lift coefficient, due to geometry symmetry, is the expected value for this aerodynamic coefficient. Tables 8 (inviscid) and 9 (viscous) present an analysis of the lift aerodynamic coefficient, based only on pressure contribution, in this study. As can be observed, the best value to the lift coefficient in the inviscid case is obtained by the LGL collocation points, coupled with the VL scheme, for the blunt body problem; and again by the LGL collocation points, coupled with the VL scheme, for the reentry capsule problem. In the viscous case, the best value to the lift coefficient is obtained by the LGL collocation points, coupled with the VL scheme, for the blunt body problem; and by the CGR collocation points, coupled

with the VL scheme, for the reentry capsule problem.

8.6. Computational Performance

Tables 10 and 11 present the computational data of the VL and LS schemes for the blunt body, for the double ellipse, and for the reentry capsule problems in both inviscid and viscous cases. It shows the CFL number and the number of iterations to convergence for all studied cases in the current work. It can be verified that the best performance of the VL scheme in the inviscid case occurred when using the CGL collocation points, employing a CFL of 0.70, and converging in 222 iterations, in the blunt body problem, whereas in the viscous case occurred when using the LGR collocation points, employing a CFL of 0.30, and converging in 359 iterations, also in the blunt body problem. On the other hand, the best performance of the LS scheme in the inviscid case occurred when using the LGR collocation points, employing a CFL of 0.50, and converging in 274 iterations, in the blunt body problem, whereas in the viscous case occurred when using the LGR collocation points, employing a CFL of 0.50, and converging in 224 iterations, also in the blunt body problem.

As final conclusion, it is possible to highlight that, for the blunt body problem, the VL scheme in the inviscid case using CGR collocation points had the best performance in estimating the stagnation pressure, and the lift aerodynamic coefficient was best estimated by the VL scheme as using the LGL collocation points also in the inviscid case; for the double ellipse problem, the VL scheme in the viscous case using CGR collocation points had the best performance in estimating the stagnation pressure; and finally, for the reentry capsule problem, the LS scheme in the viscous case using CGL collocation points had the best performance in estimating the stagnation pressure, and the lift aerodynamic coefficient was best estimated by the VL scheme as using the CGR collocation points also in the viscous case. Moreover, the best performance of the numerical schemes, for the 4^{th}order of accuracy, was due to the VL one, when using the CGL collocation points, employing a CFL of 0.70, and converging in 222 iterations, in the blunt body problem, whereas for the 16^{th} order of accuracy, the best performance of the numerical schemes was due to the LS one, when using the LGR collocation points, employing a CFL of 0.50, and converging in 224 iterations, also in the blunt body problem.

Finally, to close this work, the computational cost of the numerical schemes using the several types of collocation points is presented in Tab. 12. For the inviscid case, the cheapest combination was the VL scheme using CGL collocation points with a cost of 0.0002387 sec/per-volume/per-iteration, whereas for the viscous case the cheapest was due to the VL scheme coupled with the LGL collocation points with a cost of 0.0011181 sec/per-volume/per-iteration.

Table 1: Values of S_x and S_y

Surface	S_x	S_y
i,j-1/2	$(y_{i+1,j} - y_{i,j})$	$(x_{i,j} - x_{i+1,j})$
i+1/2,j	$(y_{i+1,j+1} - y_{i+1,j})$	$(x_{i+1,j} - x_{i+1,j+1})$
i,j+1/2	$(y_{i,j+1} - y_{i+1,j+1})$	$(x_{i+1,j+1} - x_{i,j+1})$
i-1/2,j	$(y_{i,j} - y_{i,j+1})$	$(x_{i,j+1} - x_{i,j})$

Table 2: Initial conditions to the blunt body problem

Property	Value
$M_{initial}$	8.78
$\rho_{initial}$	0.00326 kg/m^3
$pr_{initial}$	687 Pa
$U_{initial}$	4,776 m/s
$T_{initial}$	694 K
Altitude	40,000 m
c_N	10^{-9}
c_O	0.07955
c_{O2}	0.13400
c_{NO}	0.05090
c_{NO+}	0.0
c_{e-}	0.0

L_{REF}	2.0 m
Re_{char}	$2.386x10^6$

Table 3: Initial conditions to the double ellipse problem

Property	Value
$M_{initial}$	15.0
$\rho_{initial}$	0.00922 kg/m^3
$pr_{initial}$	794 Pa
$U_{initial}$	5,208 m/s
$T_{initial}$	300 K
Altitude	50,000 m
c_N	10^{-9}
c_O	0.07955
c_{O2}	0.13400
c_{NO}	0.05090
c_{NO+}	0.0
c_{e-}	0.0
L	5.0 m
Re_{char}	$1.574x10^6$

Table 4: Initial conditions to the reentry capsule problem

Property	**Value**
$M_{initial}$	10.6
$\rho_{initial}$	0.02863 kg/m^3
$pr_{initial}$	3,885 Pa
$U_{initial}$	4,628 m/s
$T_{initial}$	473 K
Altitude	40,000 m
c_N	10^{-9}
c_O	0.07955
c_{O2}	0.13400
c_{NO}	0.05090
c_{NO+}	0.0
c_{e-}	0.0
L	3.0 m
Re_{char}	$3.468x10^6$

Table 5: Values of theoretical stagnation pressure

Problem:	**$M_{initial}$:**	**pr_0/pr_∞:**	**pr_∞:**	**pr_0 (Theoretical):**
Blunt body	8.78	99.98	1.709	170.87
Double ellipse	15.00	290.20	7.109	2,063.03
Reentry capsule	10.60	145.46	9.664	1,405.73

Table 6: Values of stagnation pressure and respective errors (Inviscid case/4th Order)

Physical Problem:	**Scheme:**	**Spectral Method:**	**pr_0: (Numerical)**	**Error:**
Blunt Body (pr_0 = 170.87)	VL$^{(1)}$	Chebyshev-Gauss-Radau	171.26	0.23
	LS$^{(2)}$	Chebyshev-Gauss-Radau	169.97	0.53
	VL	Chebyshev-Gauss-Lobatto	149.43	12.55
	LS	Chebyshev-Gauss-Lobatto	153.67	10.07
	VL	Legendre-Gauss-Radau	108.33	36.60
	LS	Legendre-Gauss-Radau	129.26	24.35
	VL	Legendre-Gauss-Lobatto	119.48	30.08
	LS	Legendre-Gauss-Lobatto	135.52	20.69
	VL	Chebyshev-Gauss-Radau	1,976.37	4.20
	LS	Chebyshev-Gauss-Radau	2,007.04	2.71
	VL	Chebyshev-Gauss-Lobatto	1,729.61	16.16

Double Ellipse (pr_0 = 2,063.03)	LS	Chebyshev-Gauss-Lobatto	1,826.03	11.49
	VL	Legendre-Gauss-Radau	1,430.46	30.66
	LS	Legendre-Gauss-Radau	1,561.44	24.31
	VL	Legendre-Gauss-Lobatto	1,552.29	24.76
	LS	Legendre-Gauss-Lobatto	1,616.46	21.65
	VL	Chebyshev-Gauss-Radau	1,485.22	5.65
	LS	Chebyshev-Gauss-Radau	1,476.91	5.06
	VL	Chebyshev-Gauss-Lobatto	1,314.23	6.51
Reentry Capsule (pr_0 = 1,405.73)	LS	Chebyshev-Gauss-Lobatto	1,341.75	4.55
	VL	Legendre-Gauss-Radau	1,051.35	25.21
	LS	Legendre-Gauss-Radau	1,163.45	17.24
	VL	Legendre-Gauss-Lobatto	1,115.11	20.67
	LS	Legendre-Gauss-Lobatto	1,205.70	14.23

(1): Van Leer; (2): Liou and Steffen Jr.

Table 7: Values of stagnation pressure and respective errors (Viscous case/16th Order)

Physical Problem:	Scheme:	Spectral Method:	pr_0: (Numerical)	Error:
Blunt Body (pr_0 = 170.87)	VL	Chebyshev-Gauss-Radau	184.89	8.21
	LS	Chebyshev-Gauss-Radau	176.71	3.42
	VL	Chebyshev-Gauss-Lobatto	178.02	4.18
	LS	Chebyshev-Gauss-Lobatto	173.22	1.38
	VL	Legendre-Gauss-Radau	134.27	21.42
	LS	Legendre-Gauss-Radau	145.43	14.89
	VL	Legendre-Gauss-Lobatto	134.60	21.23
	LS	Legendre-Gauss-Lobatto	145.65	14.76
Double Ellipse (pr_0 = 2,063.03)	VL	Chebyshev-Gauss-Radau	2,057.21	0.28
	LS	Chebyshev-Gauss-Radau	2,010.07	2.57
	VL	Chebyshev-Gauss-Lobatto	1,980.71	3.99
	LS	Chebyshev-Gauss-Lobatto	1,957.57	5.11
	VL	Legendre-Gauss-Radau	1,513.28	26.65
	LS	Legendre-Gauss-Radau	1,671.85	18.96
	VL	Legendre-Gauss-Lobatto	1,516.80	26.48
	LS	Legendre-Gauss-Lobatto	1,674.13	18.85
Reentry Capsule (pr_0 = 1,405.73)	VL	Chebyshev-Gauss-Radau	1,516.36	7.87
	LS	Chebyshev-Gauss-Radau	1,462.72	4.05
	VL	Chebyshev-Gauss-Lobatto	1,465.82	4.27
	LS	Chebyshev-Gauss-Lobatto	1,427.05	1.52
	VL	Legendre-Gauss-Radau	1,122.29	20.16
	LS	Legendre-Gauss-Radau	1,217.90	13.36
	VL	Legendre-Gauss-Lobatto	1,124.82	19.98
	LS	Legendre-Gauss-Lobatto	1,219.58	13.24

Table 8: Values of the lift aerodynamic coefficient (Inviscid case/4th Order)

Physical Problem:	Scheme:	Spectral Method:	c_L:
Blunt Body	VL	Chebyshev-Gauss-Radau	-2.9327×10^{-15}
	LS	Chebyshev-Gauss-Radau	1.5459×10^{-14}
	VL	Chebyshev-Gauss-Lobatto	1.6470×10^{-14}
	LS	Chebyshev-Gauss-Lobatto	-1.2491×10^{-13}
	VL	Legendre-Gauss-Radau	2.8218×10^{-14}
	LS	Legendre-Gauss-Radau	-7.3724×10^{-14}
	VL	Legendre-Gauss-Lobatto	9.6563×10^{-16}
	LS	Legendre-Gauss-Lobatto	1.0525×10^{-14}
	VL	Chebyshev-Gauss-Radau	-2.2301×10^{-9}
	LS	Chebyshev-Gauss-Radau	-6.2623×10^{-10}

	VL	Chebyshev-Gauss-Lobatto	-1.1116×10^{-9}
Reentry Capsule	LS	Chebyshev-Gauss-Lobatto	-5.2904×10^{-10}
	VL	Legendre-Gauss-Radau	1.6647×10^{-10}
	LS	Legendre-Gauss-Radau	-2.5957×10^{-10}
	VL	Legendre-Gauss-Lobatto	-6.0024×10^{-11}
	LS	Legendre-Gauss-Lobatto	-2.6593×10^{-10}

Table 9: Values of the lift aerodynamic coefficient (Viscous case/16th Order)

Physical Problem:	Scheme:	Spectral Method:	c_L:
	VL	Chebyshev-Gauss-Radau	-2.3134×10^{-15}
	LS	Chebyshev-Gauss-Radau	2.5888×10^{-14}
	VL	Chebyshev-Gauss-Lobatto	6.5277×10^{-15}
Blunt Body	LS	Chebyshev-Gauss-Lobatto	8.7879×10^{-15}
	VL	Legendre-Gauss-Radau	3.9828×10^{-15}
	LS	Legendre-Gauss-Radau	1.9796×10^{-14}
	VL	Legendre-Gauss-Lobatto	1.4037×10^{-15}
	LS	Legendre-Gauss-Lobatto	1.6162×10^{-14}
	VL	Chebyshev-Gauss-Radau	-5.9099×10^{-11}
	LS	Chebyshev-Gauss-Radau	-3.9657×10^{-4}
	VL	Chebyshev-Gauss-Lobatto	-6.0566×10^{-11}
Reentry Capsule	LS	Chebyshev-Gauss-Lobatto	-3.5919×10^{-4}
	VL	Legendre-Gauss-Radau	-2.1631×10^{-10}
	LS	Legendre-Gauss-Radau	-1.5175×10^{-4}
	VL	Legendre-Gauss-Lobatto	-2.2428×10^{-10}
	LS	Legendre-Gauss-Lobatto	-1.5625×10^{-4}

Table 10: Computational data (Inviscid case/4th Order)

Physical Problem:	Scheme:	Spectral Method:	CFL:	Iterations:
	VL	Chebyshev-Gauss-Radau	0.50	662
	LS	Chebyshev-Gauss-Radau	0.70	358
	VL	Chebyshev-Gauss-Lobatto	0.70	222
Blunt Body	LS	Chebyshev-Gauss-Lobatto	0.70	286
	VL	Legendre-Gauss-Radau	0.50	232
	LS	Legendre-Gauss-Radau	0.50	274
	VL	Legendre-Gauss-Lobatto	0.50	233
	LS	Legendre-Gauss-Lobatto	0.50	301
	VL	Chebyshev-Gauss-Radau	0.20	1,348
	LS	Chebyshev-Gauss-Radau	0.20	1,320
	VL	Chebyshev-Gauss-Lobatto	0.20	967
Double Ellipse	LS	Chebyshev-Gauss-Lobatto	0.30	672
	VL	Legendre-Gauss-Radau	0.20	523
	LS	Legendre-Gauss-Radau	0.30	371
	VL	Legendre-Gauss-Lobatto	0.20	639
	LS	Legendre-Gauss-Lobatto	0.30	441
	VL	Chebyshev-Gauss-Radau	0.30	1,028
	LS	Chebyshev-Gauss-Radau	0.30	1,461
	VL	Chebyshev-Gauss-Lobatto	0.30	906
Reentry Capsule	LS	Chebyshev-Gauss-Lobatto	0.30	1,118
	VL	Legendre-Gauss-Radau	0.30	478
	LS	Legendre-Gauss-Radau	0.30	681

	VL	Legendre-Gauss-Lobatto	0.30	653
	LS	Legendre-Gauss-Lobatto	0.30	779

Table 11: Computational data (Viscous case/16th Order)

Physical Problem:	Scheme:	Spectral Method:	CFL:	Iterations:
Blunt Body	VL	Chebyshev-Gauss-Radau	0.50	558
	LS	Chebyshev-Gauss-Radau	0.70	349
	VL	Chebyshev-Gauss-Lobatto	0.50	506
	LS	Chebyshev-Gauss-Lobatto	0.70	324
	VL	Legendre-Gauss-Radau	0.30	359
	LS	Legendre-Gauss-Radau	0.50	224
	VL	Legendre-Gauss-Lobatto	0.30	364
	LS	Legendre-Gauss-Lobatto	0.50	225
Double Ellipse	VL	Chebyshev-Gauss-Radau	0.20	2,680
	LS	Chebyshev-Gauss-Radau	0.30	1,692
	VL	Chebyshev-Gauss-Lobatto	0.20	2,303
	LS	Chebyshev-Gauss-Lobatto	0.30	1,574
	VL	Legendre-Gauss-Radau	0.10	2,153
	LS	Legendre-Gauss-Radau	0.20	1,339
	VL	Legendre-Gauss-Lobatto	0.10	2,116
	LS	Legendre-Gauss-Lobatto	0.20	1,346
Reentry Capsule	VL	Chebyshev-Gauss-Radau	0.10	4,318
	LS	Chebyshev-Gauss-Radau	0.20	2,671
	VL	Chebyshev-Gauss-Lobatto	0.10	3,927
	LS	Chebyshev-Gauss-Lobatto	0.20	2,570
	VL	Legendre-Gauss-Radau	0.10	1,831
	LS	Legendre-Gauss-Radau	0.10	2,271
	VL	Legendre-Gauss-Lobatto	0.10	1,846
	LS	Legendre-Gauss-Lobatto	0.10	2,281

Table 12: Computational cost of spectral variants

Order of Accuracy:	Scheme:	Spectral Method:	Computational Cost (seconds/volumes/iterations):
4th Order (Inviscid case)	VL	Chebyshev-Gauss-Radau	0.0002401
	LS	Chebyshev-Gauss-Radau	0.0002390
	VL	Chebyshev-Gauss-Lobatto	0.0002387
	LS	Chebyshev-Gauss-Lobatto	0.0002388
	VL	Legendre-Gauss-Radau	0.0002977
	LS	Legendre-Gauss-Radau	0.0002979
	VL	Legendre-Gauss-Lobatto	0.0002510
	LS	Legendre-Gauss-Lobatto	0.0002639
16th Order (Viscous case)	VL	Chebyshev-Gauss-Radau	0.0011211
	LS	Chebyshev-Gauss-Radau	0.0011234
	VL	Chebyshev-Gauss-Lobatto	0.0013643
	LS	Chebyshev-Gauss-Lobatto	0.0013591
	VL	Legendre-Gauss-Radau	0.0013632
	LS	Legendre-Gauss-Radau	0.0011196
	VL	Legendre-Gauss-Lobatto	0.0011181
	LS	Legendre-Gauss-Lobatto	0.0011251

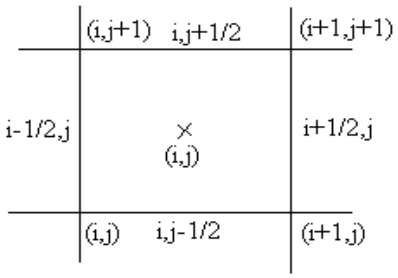

Figure 1: Computational cell

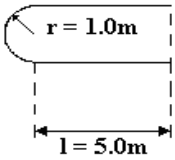

Figure 2: Blunt body configuration

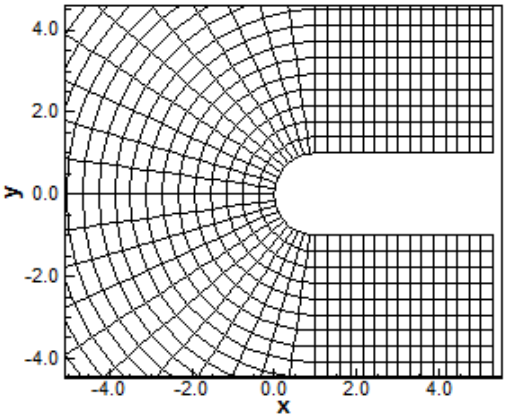

Figure 3: Blunt body inviscid mesh

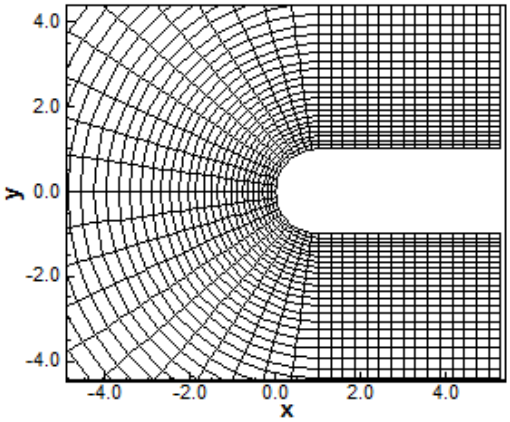

Figure 4: Blunt body viscous mesh

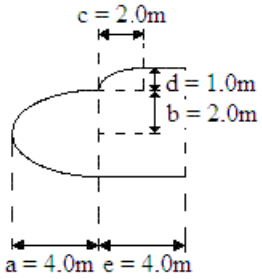

Figure 5: Double ellipse configuration

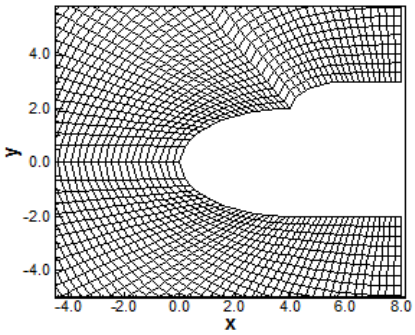

Figure 6: Double ellipse inviscid mesh

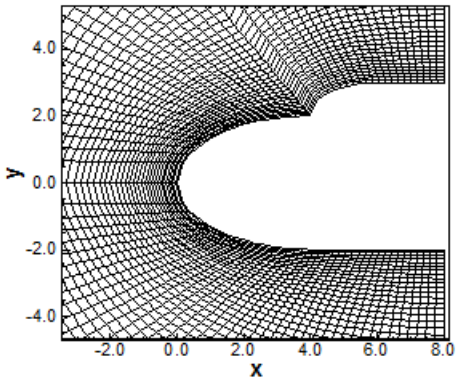

Figure 7: Double ellipse viscous mesh

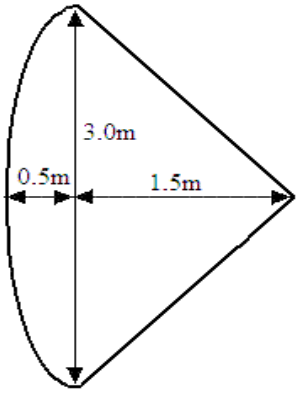

Figure 8: Reentry capsule configuration

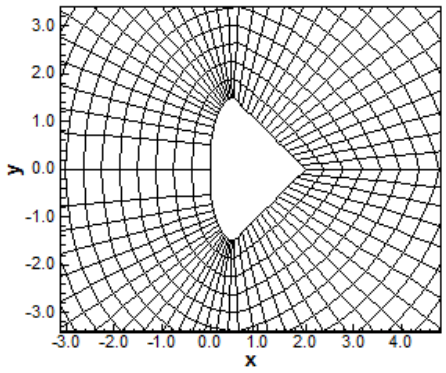

Figure 9: Reentry capsule inviscid mesh

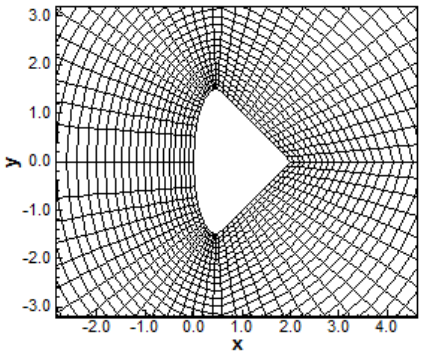

Figure 10: Reentry capsule viscous mesh

Blunt Body Inviscid Solutions

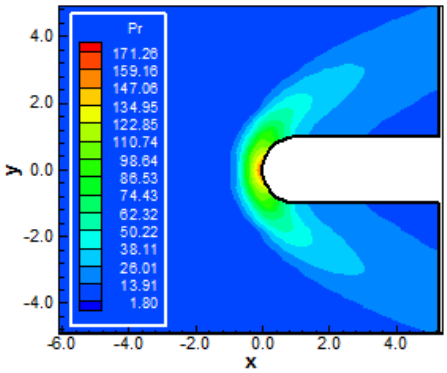

Figure 11: Pressure contours (CGR-VL)

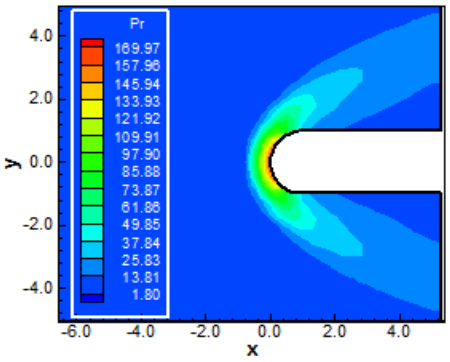

Figure 12: Pressure contours (CGR-LS)

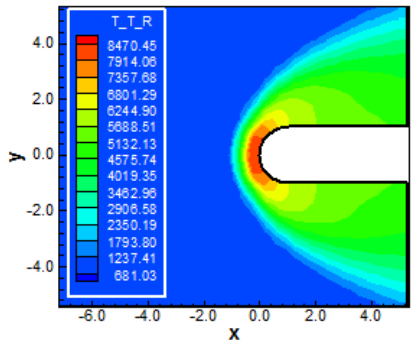

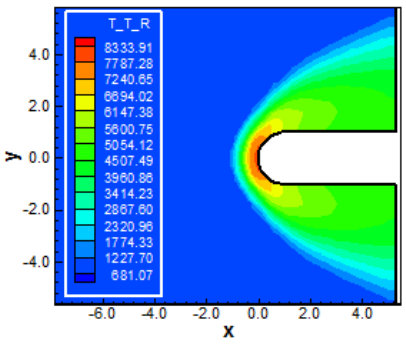

Figure 13: Translational/rotational temperature contours (CGR-VL)

Figure 14: Translational/rotational temperature contours (CGR-LS)

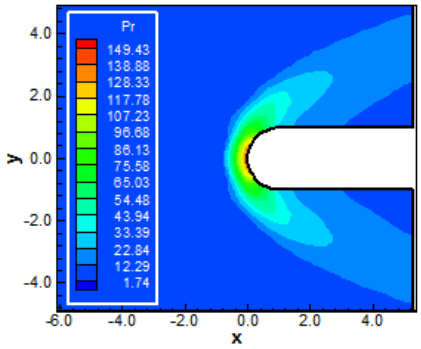

Figure 15: Pressure contours (CGL-VL)

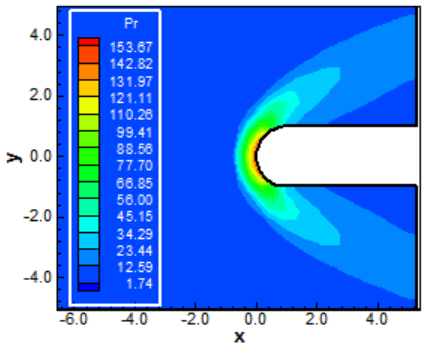

Figure 16: Pressure contours (CGL-LS)

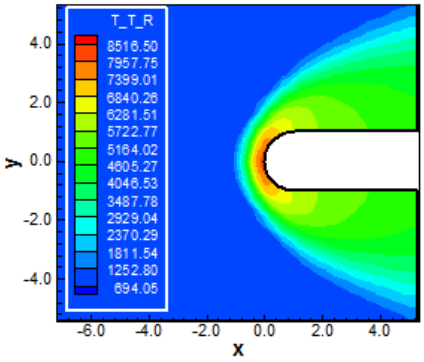

Figure 17: Translational/rotational temperature contours (CGL-VL)

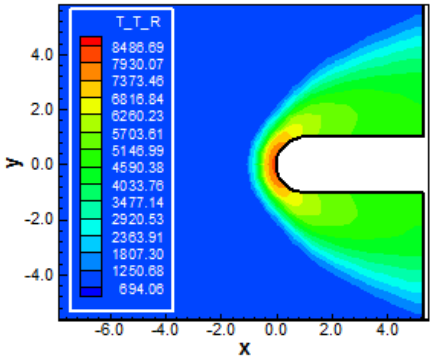

Figure 18: Translational/rotational temperature contours (CGL-LS)

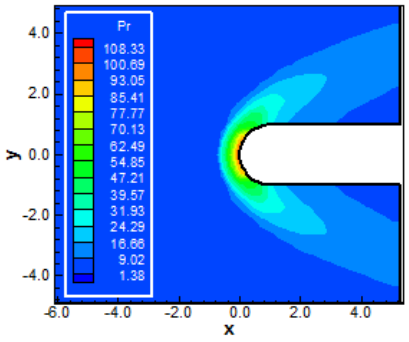

Figure 19: Pressure contours (LGR-VL)

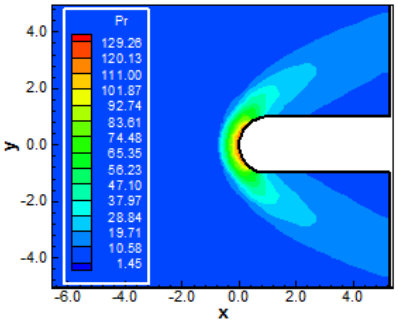

Figure 20: Pressure contours (LGR-LS)

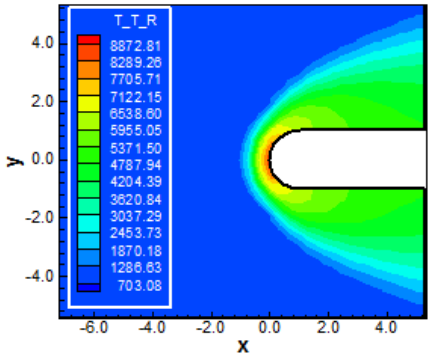

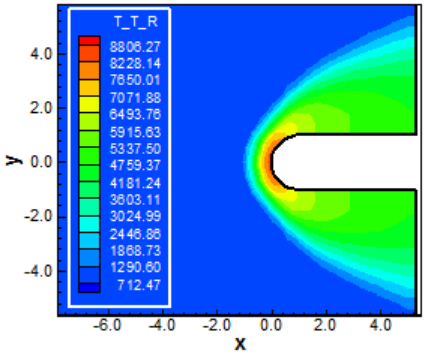

Figure 21: Translational/rotational temperature contours (LGR-VL)

Figure 22: Translational/rotational temperature contours (LGR-LS)

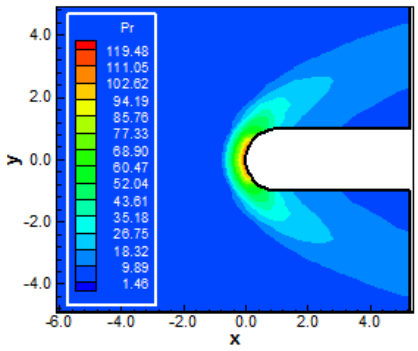

Figure 23: Pressure contours (LGL-VL)

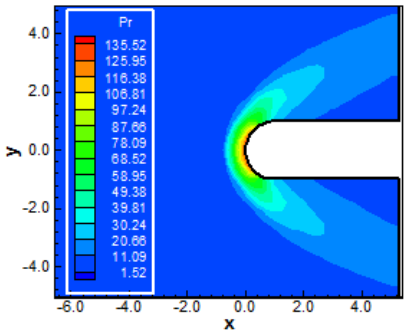

Figure 24: Pressure contours (LGL-LS)

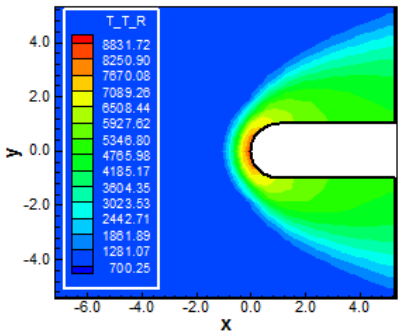

Figure 25: Translational/rotational temperature contours (LGL-VL)

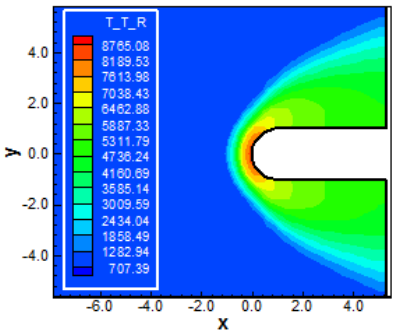

Figure 26: Translational/rotational temperature contours (LGL-LS)

Blunt Body Viscous Solutions

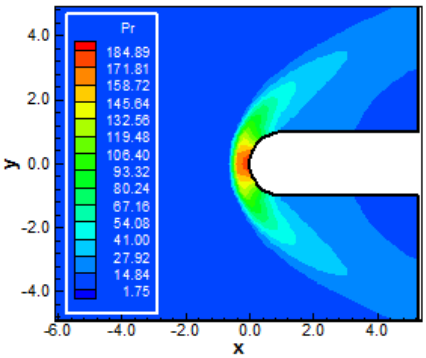

Figure 27: Pressure contours (CGR-VL)

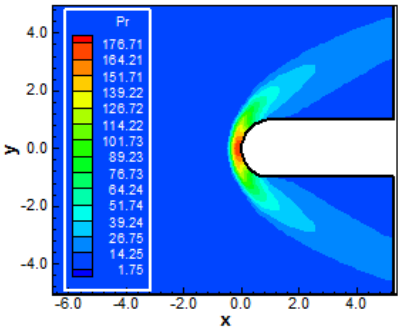

Figure 28: Pressure contours (CGR-LS)

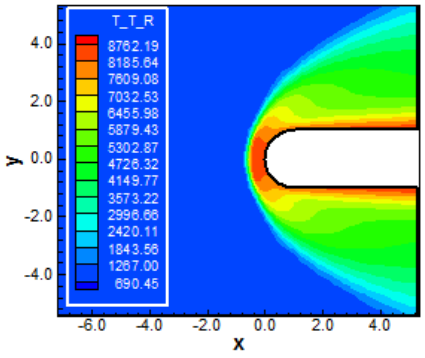

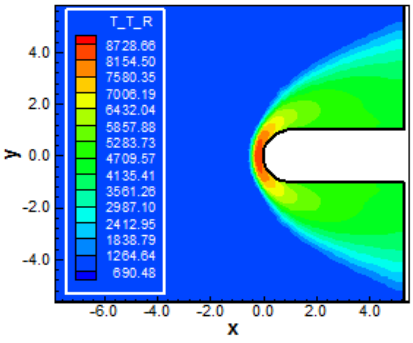

Figure 29: Translational/rotational temperature contours (CGR-VL)

Figure 30: Translational/rotational temperature contours (CGR-LS)

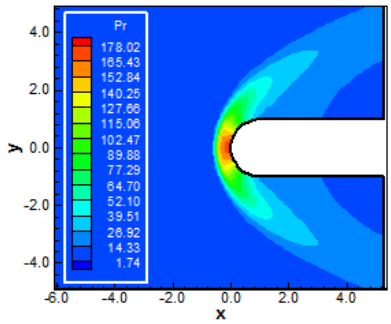

Figure 31: Pressure contours (CGL-VL)

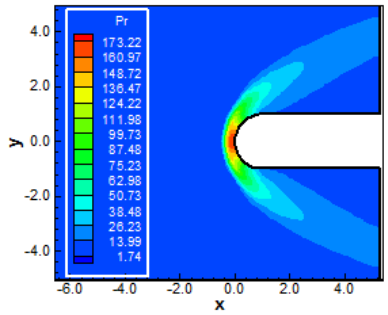

Figure 32: Pressure contours (CGL-LS)

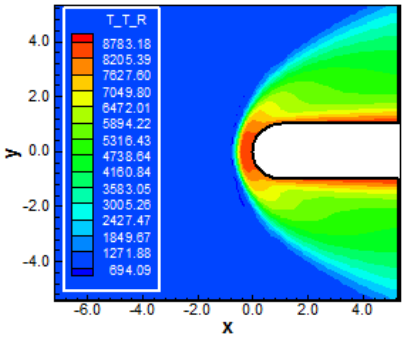

Figure 33: Translational/rotational temperature contours (CGL-VL)

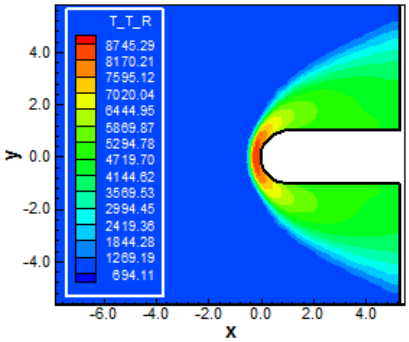

Figure 34: Translational/rotational temperature contours (CGL-LS)

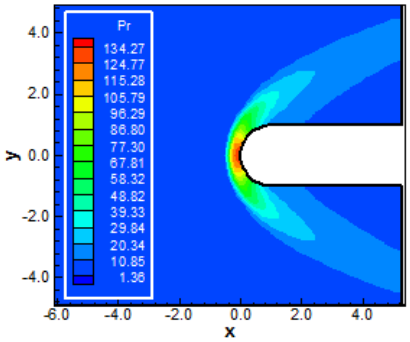

Figure 35: Pressure contours (LGR-VL)

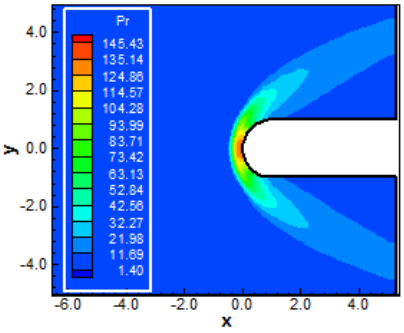

Figure 36: Pressure contours (LGR-LS)

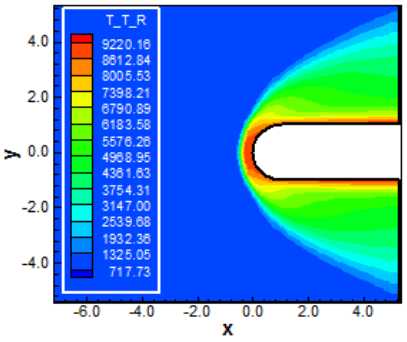

Figure 37: Translational/rotational temperature contours (LGR-VL)

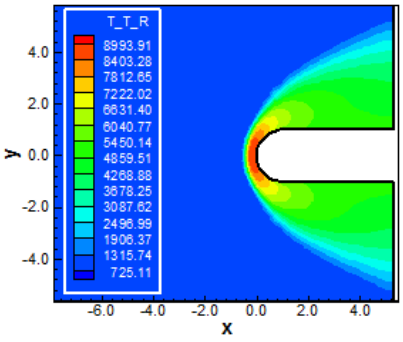

Figure 38: Translational/rotational temperature contours (LGR-LS)

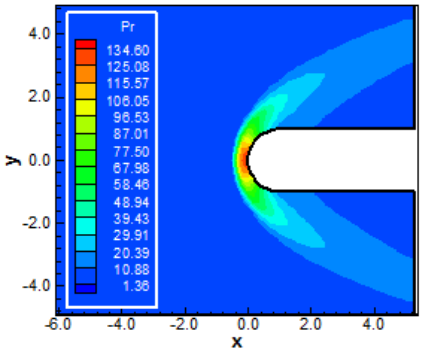

Figure 39: Pressure contours (LGL-VL)

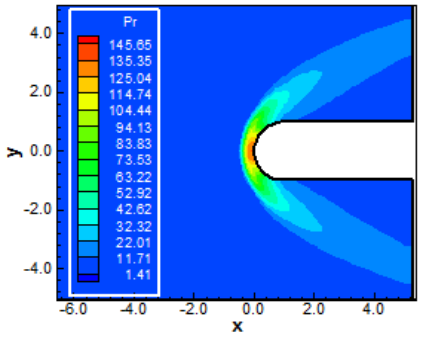

Figure 40: Pressure contours (LGL-LS)

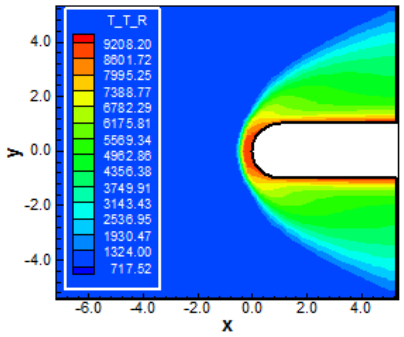

Figure 41: Translational/rotational temperature contours (LGL-VL)

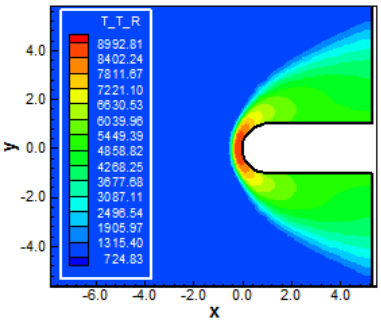

Figure 42: Translational/rotational temperature contours (LGL-LS)

Double Ellipse Inviscid Solutions

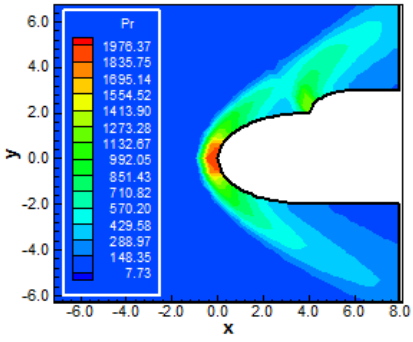

Figure 43: Pressure contours (CGR-VL)

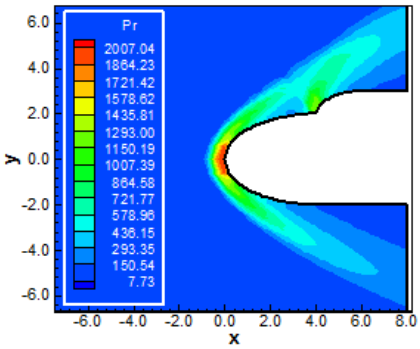

Figure 44: Pressure contours (CGR-LS)

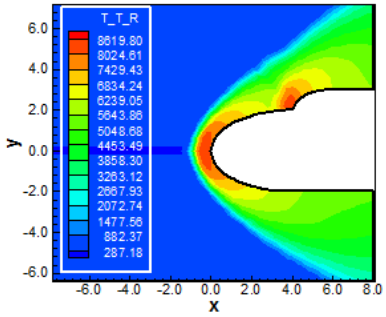

Figure 45: Translational/rotational temperature contours (CGR-VL)

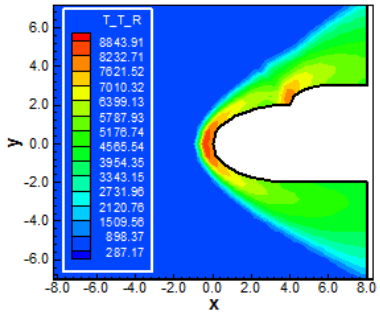

Figure 46: Translational/rotational temperature contours (CGR-LS)

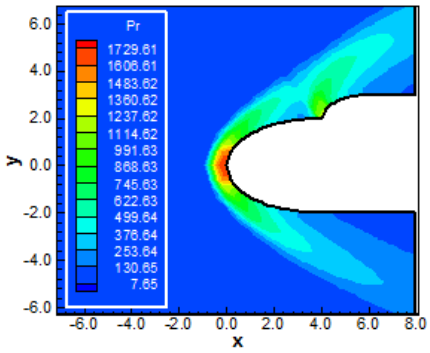

Figure 47: Pressure contours (CGL-VL)

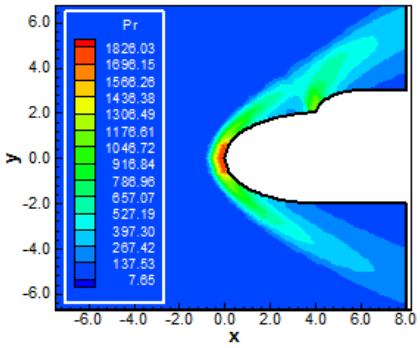

Figure 48: Pressure contours (CGL-LS)

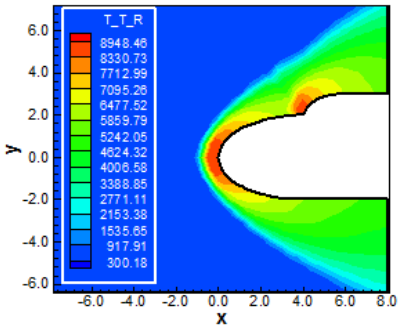

Figure 49: Translational/rotational temperature contours (CGL-VL)

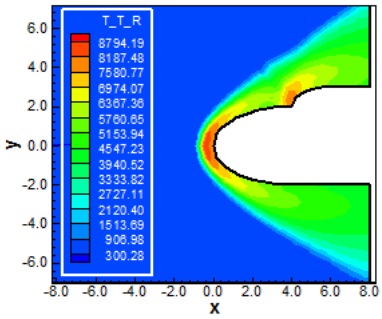

Figure 50: Translational/rotational temperature contours (CGL-LS)

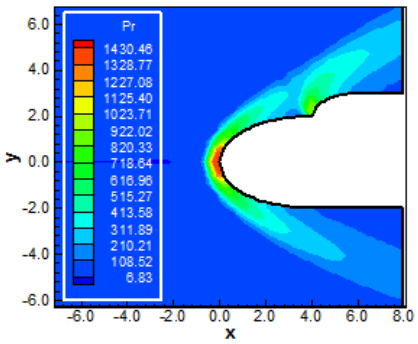

Figure 51: Pressure contours (LGR-VL)

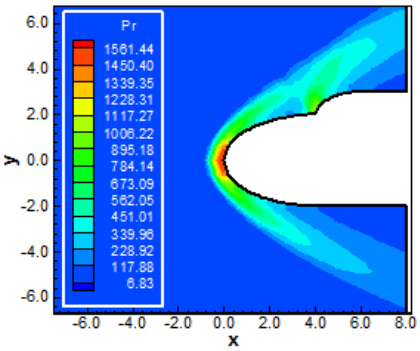

Figure 52: Pressure contours (LGR-LS)

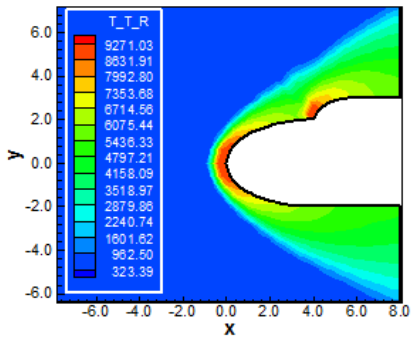

Figure 53: Translational/rotational temperature contours (LGR-VL)

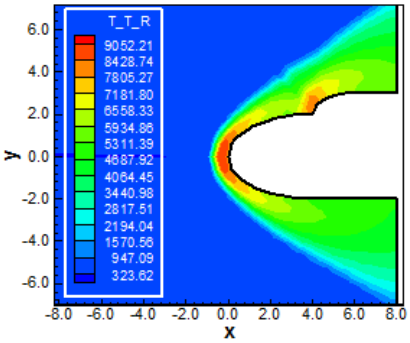

Figure 54: Translational/rotational temperature contours (LGR-LS)

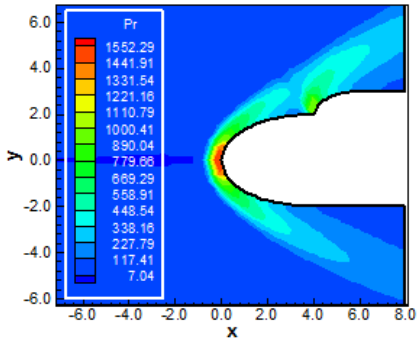

Figure 55: Pressure contours (LGL-VL)

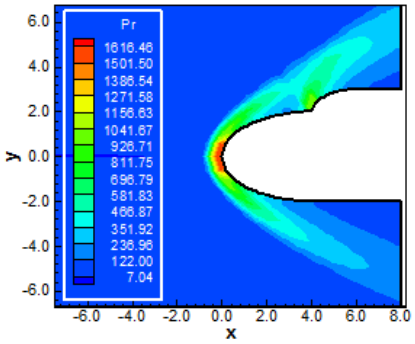

Figure 56: Pressure contours (LGL-LS)

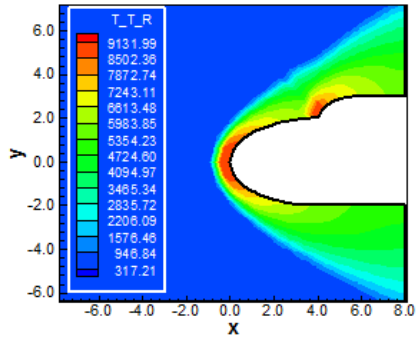

Figure 57: Translational/rotational temperature contours (LGL-VL)

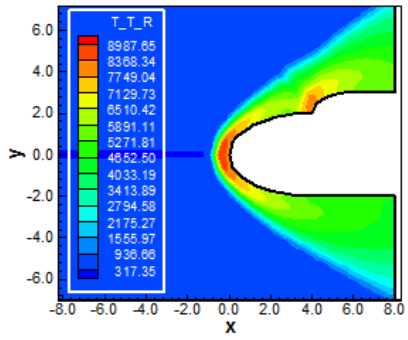

Figure 58: Translational/rotational temperature contours (LGL-LS)

Double Ellipse Viscous Solutions

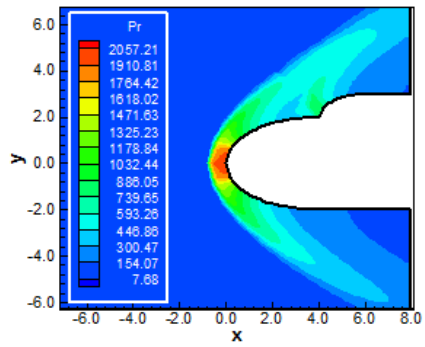

Figure 59: Pressure contours (CGR-VL)

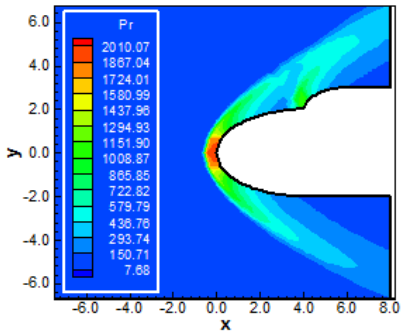

Figure 60: Pressure contours (CGR-LS)

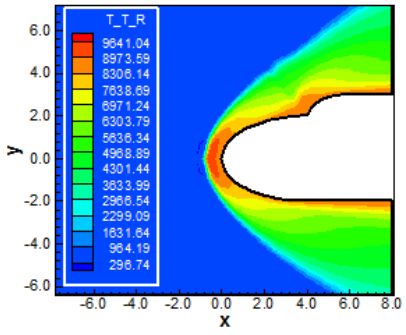

Figure 61: Translational/rotational temperature contours (CGR-VL)

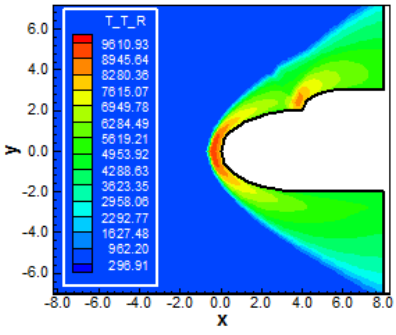

Figure 62: Translational/rotational temperature contours (CGR-LS)

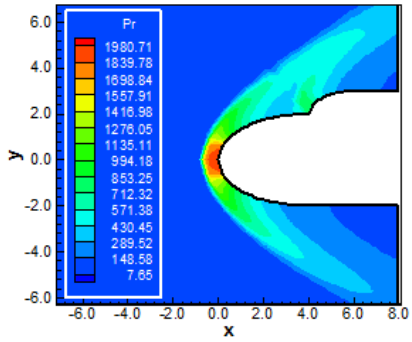

Figure 63: Pressure contours (CGL-VL)

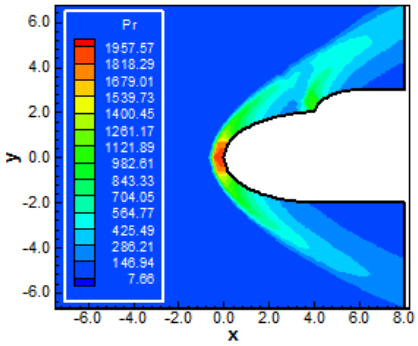

Figure 64: Pressure contours (CGL-LS)

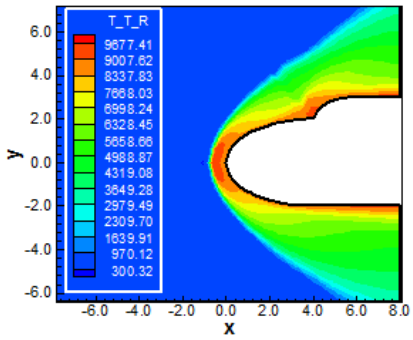

Figure 65: Translational/rotational temperature contours (CGL-VL)

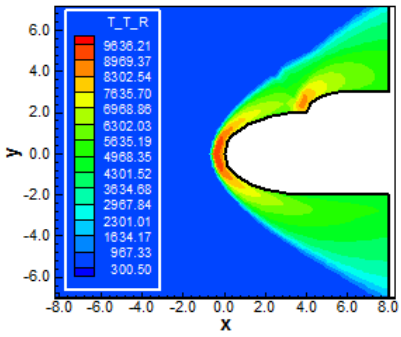

Figure 66: Translational/rotational temperature contours (CGL-LS)

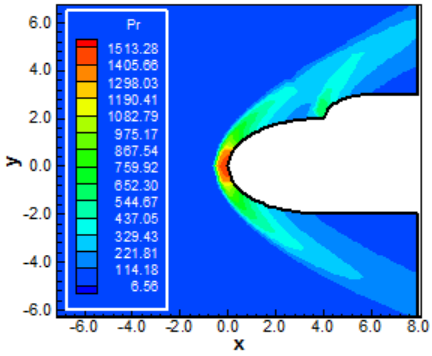

Figure 67: Pressure contours (LGR-VL)

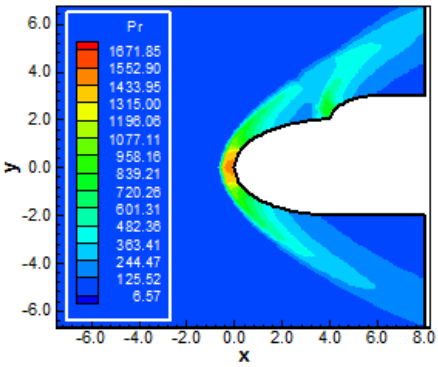

Figure 68: Pressure contours (LGR-LS)

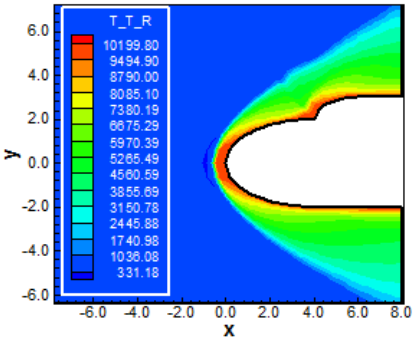

Figure 69: Translational/rotational temperature contours (LGR-VL)

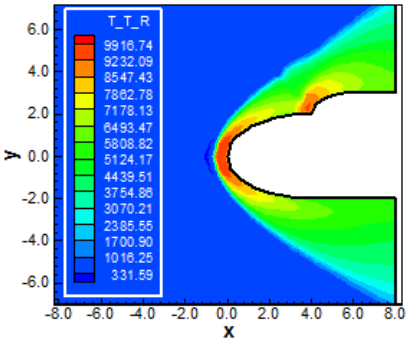

Figure 70: Translational/rotational temperature contours (LGR-LS)

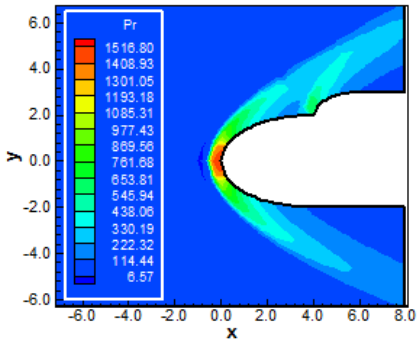

Figure 71: Pressure contours (LGL-VL)

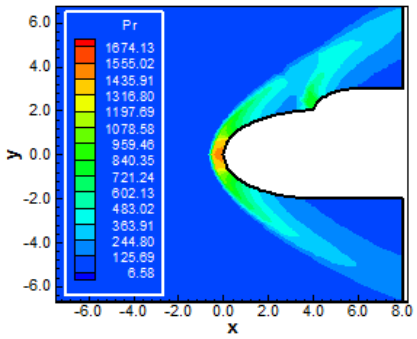

Figure 72: Pressure contours (LGL-LS)

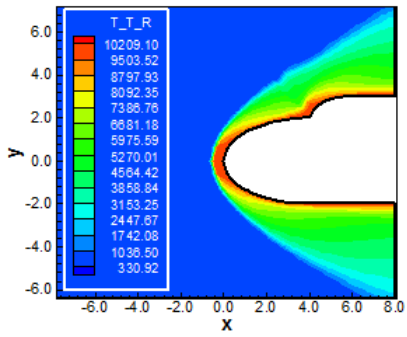

Figure 73: Translational/rotational temperature contours (LGL-VL)

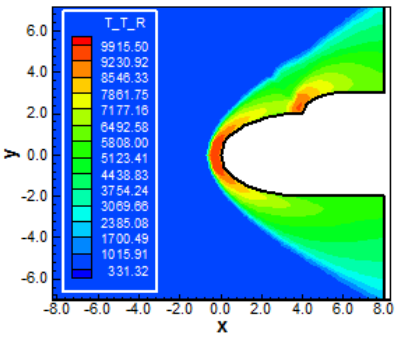

Figure 74: Translational/rotational temperature contours (LGL-LS)

Reentry Capsule Inviscid Solutions

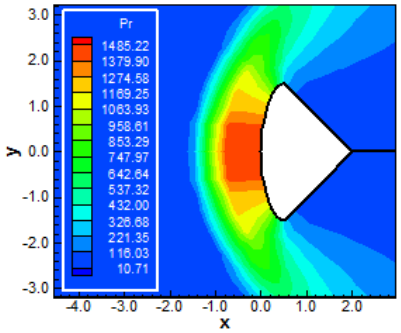

Figure 75: Pressure contours (CGR-VL)

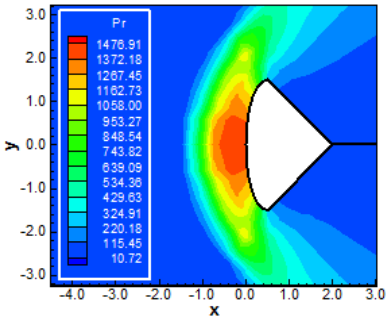

Figure 76: Pressure contours (CGR-LS).

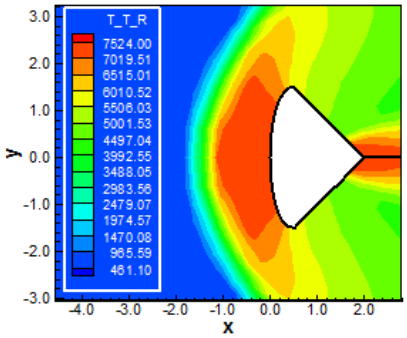

Figure 77: Translational/rotational temperature contours (CGR-VL)

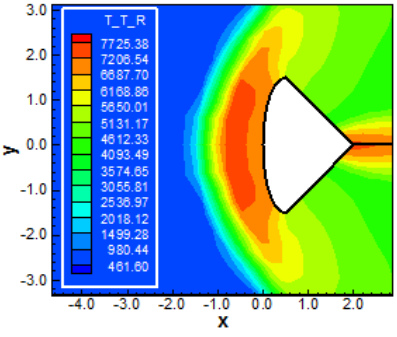

Figure 78: Translational/rotational temperature contours (CGR-LS)

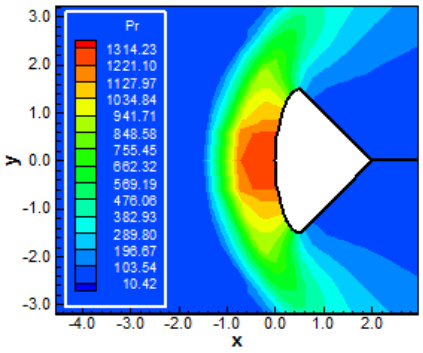

Figure 79: Pressure contours (CGL-VL)

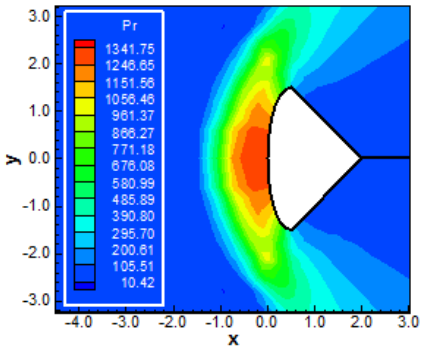

Figure 80: Pressure contours (CGL-LS)

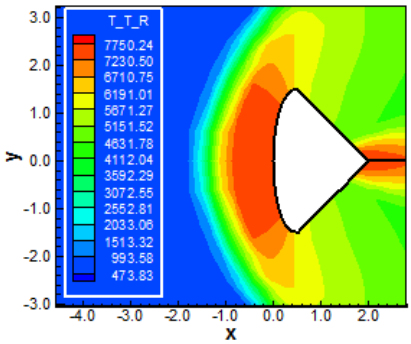

Figure 81: Translational/rotational temperature contours (CGL-VL)

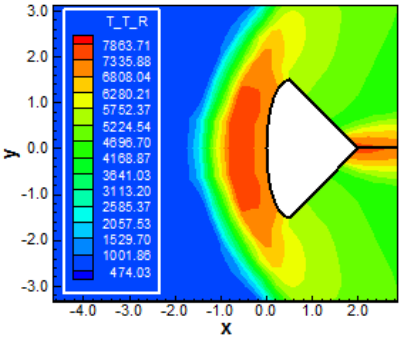

Figure 82: Translational/rotational temperature contours (CGL-LS)

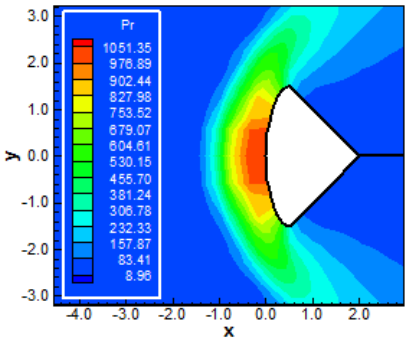

Figure 83: Pressure contours (LGR-VL)

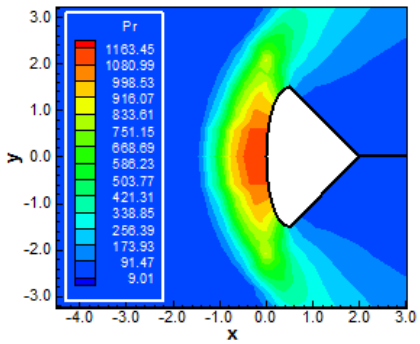

Figure 84: Pressure contours (LGR-LS)

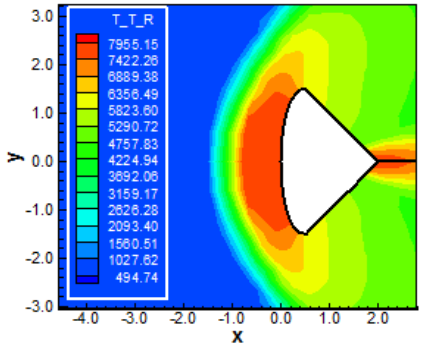

Figure 85: Translational/rotational temperature contours (LGR-VL)

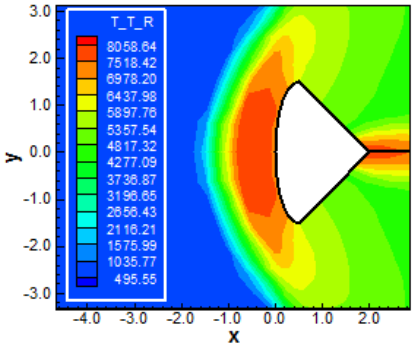

Figure 86: Translational/rotational temperature contours (LGR-LS)

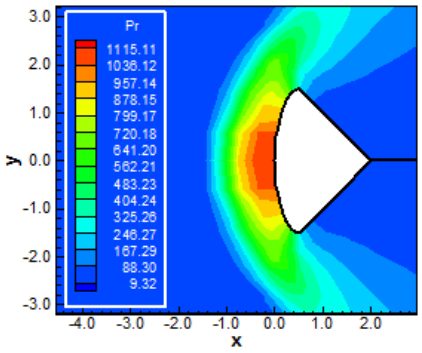

Figure 87: Pressure contours (LGL-VL)

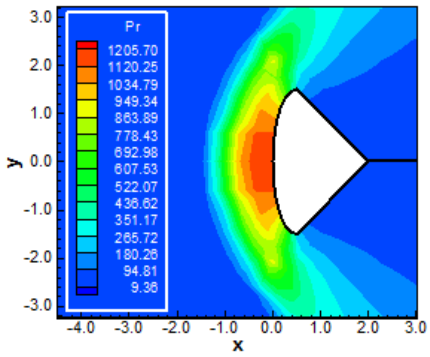

Figure 88: Pressure contours (LGL-LS)

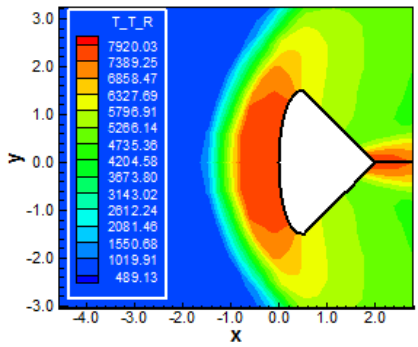

Figure 89: Translational/rotational temperature contours (LGL-VL)

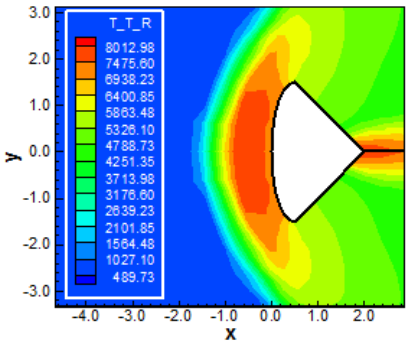

Figure 90: Translational/rotational temperature contours (LGL-LS)

Reentry Capsule Viscous Solutions

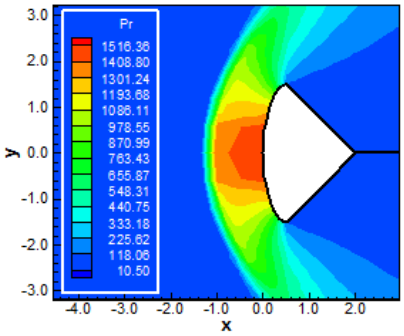

Figure 91: Pressure contours (CGR-VL)

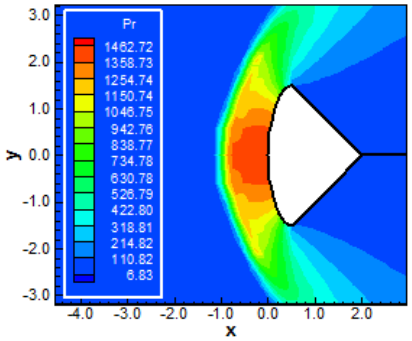

Figure 92: Pressure contours (CGR-LS).

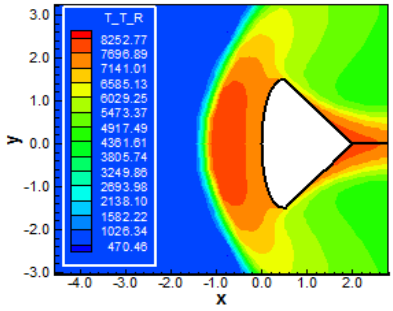

Figure 93: Translational/rotational temperature contours (CGR-VL)

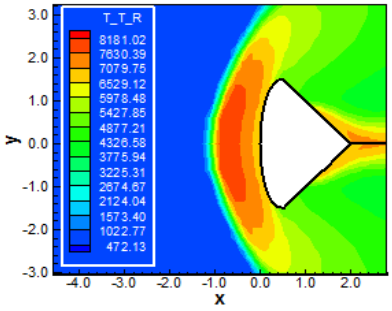

Figure 94: Translational/rotational temperature contours (CGR-LS)

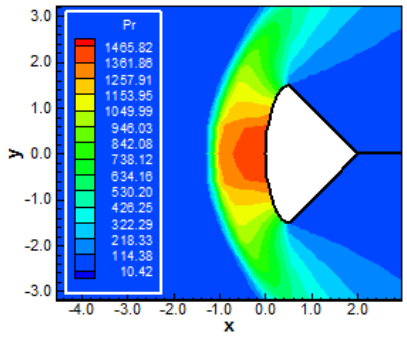

Figure 95: Pressure contours (CGL-VL)

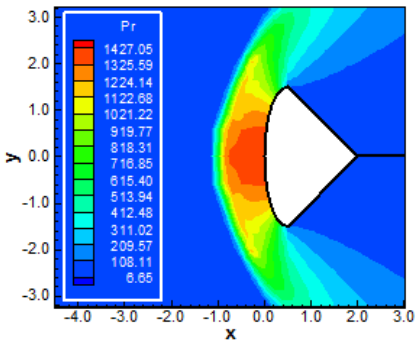

Figure 96: Pressure contours (CGL-LS)

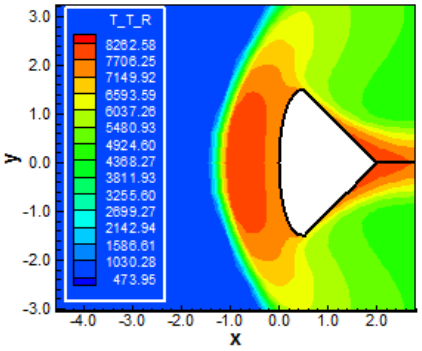

Figure 97: Translational/rotational temperature contours (CGL-VL)

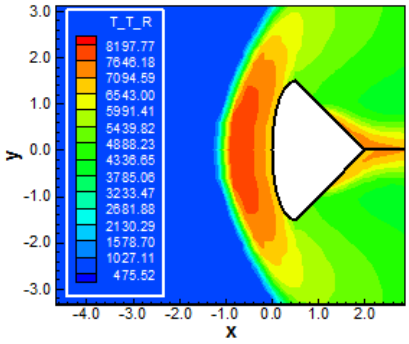

Figure 98: Translational/rotational temperature contours (CGL-LS)

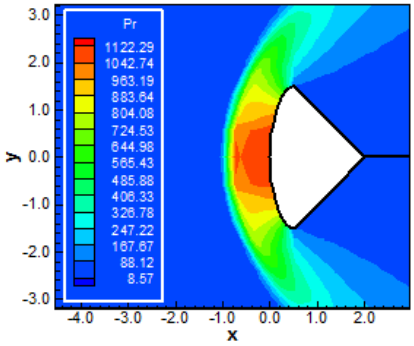

Figure 99: Pressure contours (LGR-VL)

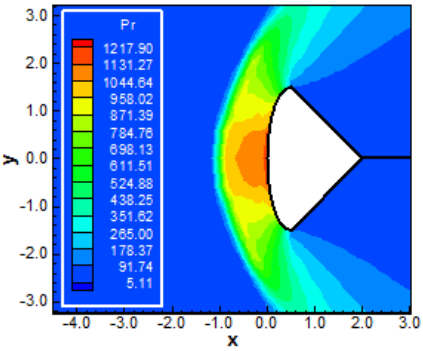

Figure 100: Pressure contours (LGR-LS)

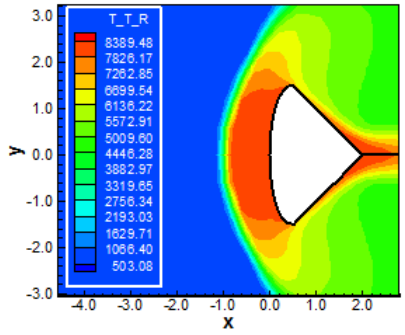

Figure 101: Translational/rotational temperature contours (LGR-VL)

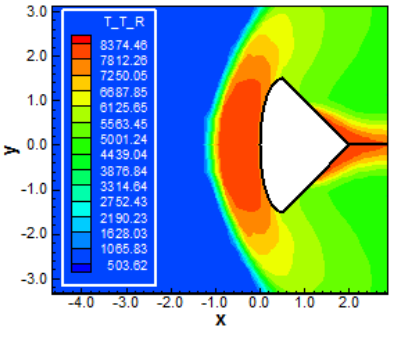

Figure 102: Translational/rotational temperature contours (LGR-LS)

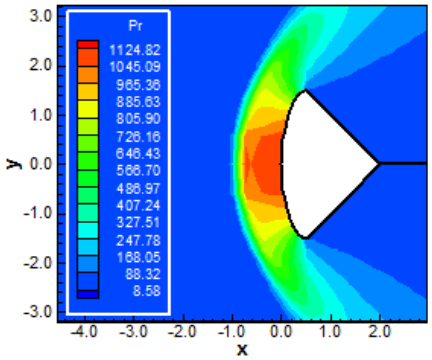

Figure 103: Pressure contours (LGL-VL)

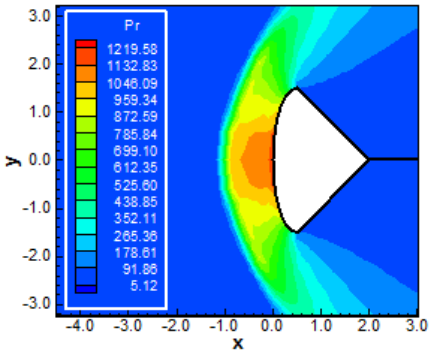

Figure 104: Pressure contours (LGL-LS)

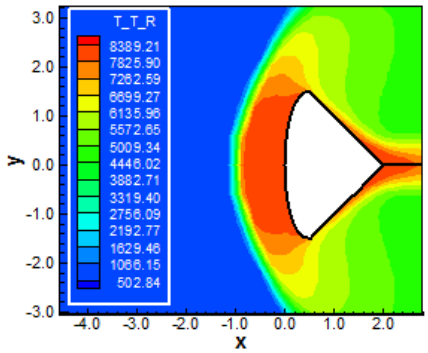

Figure 105: Translational/rotational temperature contours (LGL-VL)

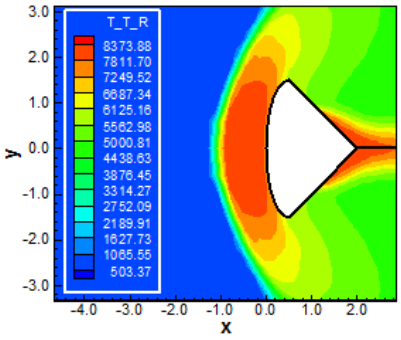

Figure 106: Translational/rotational temperature contours (LGL-LS)

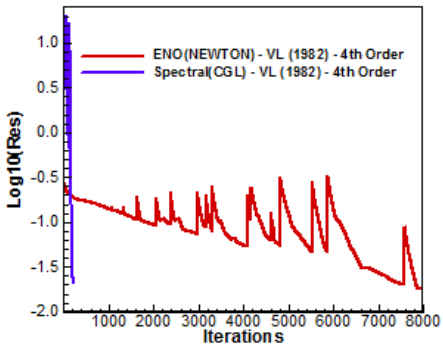

Figure 107: Comparison between convergence histories (VL)

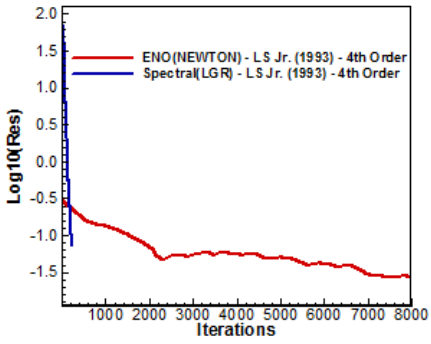

Figure 108: Comparison between convergence histories (LS)

9. Conclusions

In the present work, a study involving a spectral method to solve the reactive Euler and Navier-Stokes equations was performed. The Euler and Navier-Stokes equations, in conservative and finite volume contexts, employing structured spatial discretization, on a condition of thermochemical non-equilibrium, were studied. The spectral method presented in this work employed collocation points and variants of Chebyshev and Legendre interpolation functions were analyzed. High-order studies were accomplished to verify the accuracy of the spectral method. The "hot gas" hypersonic flows around a blunt body, around a double ellipse, and around a reentry capsule in two-dimensions were simulated. The [28-29] flux vector splitting algorithms were applied to execute the numerical experiments. The Euler backward integration method was employed to march the schemes in time. The convergence process was accelerated to steady state condition through a spatially variable time step procedure, which had proved effective gains in terms of computational acceleration [30-31]. The

reactive simulations involved Earth atmosphere chemical model of seven species and eighteen reactions, based on the [32] model. N, O, N_2, O_2, NO, NO^+, and e^- species were used to accomplish the numerical comparisons. The results have indicated that the Chebyshev collocation point variants are more accurate in terms of stagnation pressure estimations. In the inviscid case such errors were inferior to 16.16%, while in the viscous case such errors were inferior to 10.0%. The Legendre collocation point variants are more accurate in terms of the lift coefficient estimations. Moreover, the Legendre collocation point variants are more computationally efficient and cheaper.

As final conclusion, it is possible to highlight that, for the blunt body problem, the [28] scheme in the inviscid case using Chebyshev-Gauss-Radau collocation points had the best performance in estimating the stagnation pressure, and the lift aerodynamic coefficient was best estimated by the [28] scheme as using the Legendre-Gauss-Lobatto collocation points also in the inviscid case; for the double ellipse problem, the [28] scheme in the viscous case using Chebyshev-Gauss-Radau collocation points had the best performance in estimating the stagnation pressure; and finally, for the reentry capsule problem, the [29] scheme in the viscous case using Chebyshev-Gauss-Lobatto collocation points had the best performance in estimating the stagnation pressure, and the lift aerodynamic coefficient was best estimated by the [28] scheme as using the Chebyshev-Gauss-Radau collocation points also in the viscous case. Moreover, the best performance of the numerical schemes, for the 4^{th} order of accuracy, was due to the [28] one, when using the Chebyshev-Gauss-Lobatto collocation points, employing a CFL of 0.70, and converging in 222 iterations, in the blunt body problem, whereas for the 16^{th} order of accuracy, the best performance of the numerical schemes was due to the [29] one, when using the Legendre-Gauss-Radau collocation points, employing a CFL of 0.50, and converging in 224 iterations, also in the blunt body problem.

Finally, to close this work, the computational cost of the numerical schemes using the several types of collocation points was presented in Tab. 12. For the inviscid case, the cheapest combination was the [28] scheme using Chevyshev-Gauss-Lobatto collocation points with a cost of 0.0002387 sec/per-volume/per-iteration, whereas for the viscous case the cheapest was due to the [28] scheme coupled with the Legendre-Gauss-Lobatto collocation points with a cost of 0.0011181 sec/per-volume/per-iteration.

10. Motivation and Novelty

The motivation to study spectral methods applied to reentry flow was enormous because of some papers in the CFD literature report such methods as the state of art of high order resolution. The intention of this paper was to propose a different spectral method that was of easy implementation and conformed about author's ideas of treating the governing equations of fluid flow. The formulation presented here is for a thermochemical non-equilibrium condition and a two-temperature model. The comparisons involving the residual histories of ENO and of spectral method were very important to confirm that our numerical implementation was correct and also the potentiality of the method. Three physical problems were also a challenge that we accepted to lead with. The results with good accuracy represent a motivation to extend the present formulation to more species and different chemical conditions.

The novelty of the present study was to implement this different spectral method to treat thermochemical non-equilibrium reentry flows and to formulate the appropriate equations for accepting this method. The robustness and convergence features of this spectral method are very impressive. While the author had to use CFL numbers of order 0.01 for his ENO explicit method, CFL numbers as great as 0.70 for his explicit spectral method were of common use. The proposed spectral method is different from the standard spectral ones on a sense that in the latter, the differential equations and the solution method are discretized with spectral tools, whereas in the former, only the vector of conserved variables and the convective fluxes should be discretized according to the spectral tools. The result is a robust and fast solver to treat the fluid-dynamic of reentry flows.

11. Future Works

For the future, the author should extend the present formulation for an eleven species chemical model under the condition of thermochemical non-equilibrium in two-dimensions. After that, he should extend to the desired three-dimensional studies. Moreover, its implementation with turbulence effects and magnetic field actuation,

that the author consider as the state of the art project, is an objective to be reached, in both, two- and three-dimensions. Finally, the interpretation of the present formulation to two-dimensional unstructured studies is also a goal to be reached.

Acknowledgments
The author would like to thank the ITA facilities that allowed the realization of this work. He would also like to thank the CAPES by the financial support conceded under the form of a scholarship.

References

[1]. Barnes CJ, Huang GP, Shang JS. A high resolution spectral method for the compressible Navier-Stokes equations. AIAA Paper 2011-0049; 2011.
[2]. Huang P, Wang ZJ, Liu Y. An implicit space-time spectral difference method for discontinuity capturing using adaptive polynomials. AIAA Paper 2005-5255; 2005.
[3]. Huang P. High order discontinuity capturing using adaptive polynomials. AIAA Paper 2006-0305; 2006.
[4]. Steger JL, Warming RF. Flux vector splitting of the inviscid gas dynamic equations with application to finite difference methods. Journal of Computational Physics, 1981; 40: 263-293.
[5]. Hughes T. The finite element method, linear static and dynamic finite element analysis, Prentice-Hall, Inc.
[6]. Lele S. Compact finite difference schemes with spectral-like resolution. Journal of Computational Physics, 1991; 103: 16-42.
[7]. Gottlieb D, Orszag S. Numerical analysis of spectral methods: theory and applications, Society for Industrial and Applied Mathematics, Philadelphia.
[8]. Hussaini MY, Kopriva DA, Salas MD, Zang TA. Spectral methods for the Euler equations: Part I – Fourier methods and shock capturing. AIAA Journal, 1985; 23(1): 64-70.
[9]. Slater JC. Electronic energy bands in metal. Physical Review, 1934; 45: 794-801.
[10]. Barta J. Ü ber die naherungsweise l ü sung einigerzweidimensionalerelastizit ä tsaufgaben. ZeitschriftfuerAngewandteMathematik und Mechanik, 1937; 17: 184-185.
[11]. Frazer RA, Jones WP, Skan SW. Approximation to functions and to the solutions of differential equations. Aeronautical Research Council, London. R&M 1799; 1937.
[12]. Lanczos CL. Trigonometric interpolation of empirical and analytic functions. Journal of Mathematics and Physics, 1938; 17: 123-199.
[13]. Gottlieb D, Lustman L, Orszag SA. Spectral calculations of one-dimensional inviscid compressible flows. SIAM Journal of Scientific and Statistical Computation, 1981; 2: 296-310.
[14]. Taylor TD, Meyers RB, Albert JH. Pseudospectral calculations of shock waves, rarefaction waves and contact surfaces. Computers and Fluids, 1981; 9: 469-473.
[15]. Zang TA, Hussaini MY. Mixed spectral-finite difference approximations for slightly viscous flows. Proceedings of the 7th International Conference on Numerical Methods in Fluid Dynamics. Edited by W. C. Reynolds and R. W. MacCormack. Lecture Notes in Physics, Springer-Verlag, New York, 1981; (141): 461-466.
[16]. Narayan JR, Girimaji SS. Turbulent reacting flow computations including turbulence-chemistry interactions. AIAA Paper 92-0342; 1992.
[17]. Gnoffo PA, Gupta RN, Shinn JL. Conservation equations and physical models for hypersonic flows in thermal and chemical nonequilibrium. NASA TP 2867; 1989.
[18]. Liu M, Vinokur M. Upwind algorithms for general thermo-chemical nonequilibrium flows. AIAA Paper 89-0201; 1989.
[19]. Park C. Radiation enhancement by nonequilibrium in Earth's atmosphere. Journal of Spacecraft and Rockets, 1985; 22(1): 27-36.

[20]. Park C. Problem of rate chemistry in the flight regimes of aeroassissted orbital transfer vehicles. Thermal design of aeroassissted orbital transfer vehicles. Progress in Astronautics and Aeronautics. Edited by H. F. Nelson, AIAA, NY, 1985; 96: 511-537.
[21]. Gnoffo PA. Three-dimensional AOTV flowfields in chemical nonequilibrium. AIAA Paper 86-0230; 1986.
[22]. Li CP. Implicit methods for computing chemically reacting flow. NASA TM-58274; 1986.
[23]. Lee JH. Basic governing equations for the flight regimes of aeroassisted orbital transfer vehicles. Thermal design of aeroassisted transfer vehicles. Progress in Astronautics and Aeronautics, AIAA, 1985; 96: 3-53.
[24]. Park C. Convergence of computation of chemically reacting flows. Thermophysical aspects of reentry flows. Progress in Astronautics and Aeronautics. Edited by J. N. Moss and C. D. Scott, AIAA, NY, 1986; 103: 478-513.
[25]. Park C. Assessment of two-temperature kinetic model for dissociating and weakly-ionizing nitrogen. AIAA Paper 86-1347; 1986.
[26]. Park C. Calculation of nonequilibrium radiation in the flight regimes of aeroassissted orbital transfer vehicles. Thermal design of aeroassissted orbital transfer vehicles. Progress in Astronautics and Aeronautics. Edited by H. F. Nelson, AIAA, NY, 1985; 96: 395-418.
[27]. Park C. Nonequilibrium air radiation (NEQAIR) program: User's manual. NASA TM-86707; 1985.
[28]. Van Leer B. Flux-vector splitting for the Euler equations. Lecture Notes in Physics, Springer Verlag, Berlin, 1982; 170: 507-512.
[29]. Liou M, Steffen Jr. CJ. A new flux splitting scheme. Journal of Computational Physics, 1993; 107: 23-39.
[30]. Maciel ESG. Simulations in 2D and 3D applying unstructured algorithms, Euler and Navier-Stokes equations – Perfect gas formulation. Saarbrücken, Deutschland: Lambert Academic Publishing (LAP), 2015; Ch. 1: 26-47.
[31]. Maciel ESG. Simulations in 2D and 3D applying unstructured algorithms, Euler and Navier-Stokes equations – Perfect gas formulation. Saarbrücken, Deutschland: Lambert Academic Publishing (LAP), 2015; Ch. 6: 160-181.
[32]. Blottner FG. Viscous shock layer at the stagnation point with nonequilibrium air chemistry. AIAA Journal, 1969; 7(12): 2281-2288.
[33]. Hussaini MY, Streett CL, Zang TA. Spectral methods for partial differential equations. ICASE Report No. 83-46; 1983.
[34]. Davis PA, Rabinowitz P. Numerical integration, Blaisdell Publishing Co.; 1967.
[35]. Canuto C, Hussaini MY, Quarteroni A, Zang TA. Spectral methods evolution to complex geometries and applications to fluid dynamics. Scientific Computation Springer; 2007.
[36]. Prabhu RK. An implementation of a chemical and thermal nonequilibrium flow solver on unstructured meshes and application to blunt bodies. NASA CR-194967; 1994.
[37]. Saxena SK, Nair MT. An improved Roe scheme for real gas flow. AIAA Paper 2005-0587; 2005.
[38]. Maciel ESG. Hypersonic reactive flow simulations in two-dimensions, chemical and thermochemical non-equilibrium conditions. Saarbrücken. Deutschland: Lambert Academic Publishing (LAP), 2015; Ch. 5:333-406.
[39]. Maciel ESG. Hypersonic reactive flow simulations in two-dimensions, chemical and thermochemical non-equilibrium conditions. Saarbrücken. Deutschland: Lambert Academic Publishing (LAP), 2015; Ch. 6: 407-490.
[40]. Ait-Ali-Yahia D, Habashi WG. Finite element adaptive method for hypersonic thermochemical nonequilibrium flows. AIAA Journal, 1997; 35(8): 1294-1302.
[41]. Radespiel R, Kroll N. Accurate flux vector splitting for shocks and shear layers. Journal of Computational Physics, 1995; 121: 66-78.
[42]. Long LN, Khan MMS, Sharp HT. Massively parallel three-dimensional Euler / Navier-Stokes method. AIAA Journal, 1991; 29(5): 657-666.

[43]. Vincent WG, Kruger Jr. Ch. Introduction to physical gas dynamics. Malabar, Florida, EUA: Krieger Publishing Company, 2002; Ch. 1: 1-26.
[44]. Fox RW, McDonald AT. Introdução à mecânica dos fluidos. Guanabara Editor; 1988.
[45]. Maciel ESG. Simulação numérica de escoamentos supersônicos e hipersônicos utilizando técnicas de dinâmica dos fluidos computacional.Doctoralthesis, ITA, CTA, São José dos Campos, SP, Brazil; 2002.
[46]. Maciel ESG. High order comparison between flux vector splitting schemes on the reentry flow context. Computational and Applied Mathematics Journal, 2015; 1(4):225-248.
[47]. Maciel ESG. Comparison between Newton and Hermite ENO interpolations as applied to reentry flows in 2D.Computational and Applied Mathematics Journal, 2015; 1(5): 261-281.
[48]. Maciel ESG. Comparison among MUSCL, ENO and WENO procedures as applied to reentry flows in 2D. Computational and Applied Mathematics Journal, 2015; 1(5): 355-377.
[49]. Anderson Jr. JD. Fundamentals of aerodynamics, McGraw-Hill, Inc., 5th Edition, 1008p.; 2010.